

34

35 **Abstract**

36 Recycling of upper plate crust in subduction zones, or 'subduction erosion', is a major
37 mechanism of crustal destruction at convergent margins. However, assessing the impact
38 of eroded crust on arc magmas is difficult owing to the compositional similarity between
39 the eroded crust, trench sediment and arc crustal basement that may all contribute to arc
40 magma formation. Here we compare Sr-Nd-Pb-Hf and trace element data of crustal
41 input material to Sr-Nd-Pb-Hf-He-O isotope chemistry of a well-characterized series of
42 olivine-phyric, high-Mg# basalts to dacites in the central Mexican Volcanic Belt (MVB).
43 Basaltic to andesitic magmas crystallize high-Ni olivines that have high mantle-like
44 $^3\text{He}/^4\text{He} = 7-8 R_a$ and high crustal $\delta^{18}\text{O}_{\text{melt}} = +6.3-8.5\%$ implying their host magmas to be
45 near-primary melts from a mantle infiltrated by slab-derived crustal components.
46 Remarkably, their Hf-Nd isotope and Nd/Hf trace element systematics rule out the
47 trench sediment as the recycled crust end member, and imply that the coastal and
48 offshore granodiorites are the dominant recycled crust component. Sr-Nd-Pb-Hf isotope
49 modeling shows that the granodiorites control the highly to moderately incompatible
50 elements in the calc-alkaline arc magmas, together with lesser additions of Pb- and Sr-
51 rich fluids from subducted mid-oceanic ridge basalt (MORB)-type altered oceanic crust
52 (AOC). Nd-Hf mass balance suggests that the granodiorite exceeds the flux of the trench
53 sediment by at least 9-10 times, corresponding to a flux of $\geq 79-88 \text{ km}^3/\text{km}/\text{Myr}$ into the
54 subduction zone. At an estimated thickness of 1500-1700 m, the granodiorite may
55 buoyantly rise as bulk 'slab diapirs' into the mantle melt region and impose its trace
56 element signature (e.g. Th/La, Nb/Ta) on the prevalent calc-alkaline arc magmas. Deep
57 slab melting and local recycling of other slab components such as oceanic seamounts
58 further diversify the MVB magmas by producing rare, strongly fractionated high-La
59 magmas and a minor population of high-Nb magmas, respectively. Overall, the central
60 MVB magmas inherit their striking geochemical diversity principally from the slab, thus
61 emphasizing the importance of continental crust recycling in modern solid Earth relative
62 to its new formation in modern subduction zones.

63 1. **INTRODUCTION**

64 Subduction zone magmas share remarkable compositional similarities with the
65 continental crust. This has triggered a longstanding and controversial debate regarding
66 whether the continental crust was extracted from the Earth's mantle by processes similar
67 to those of modern convergent margins (e.g. Harrison, 2009; Plank, 2004; Stern, 2011;
68 Taylor, 1967). A pivotal question in this debate is the extent to which subduction

69 processing can create the typical fractionated trace element signature of the continental
70 crust, or whether this signature is mostly inherited through perpetual recycling of
71 continental crust in subduction zones (e.g. Plank, 2004; Rudnick, 1995). Continental crust
72 is recycled in subduction zones by means of the oceanic sediment subducted at the
73 trenches ('trench sediment') and by subduction erosion of the upper plate crust (Clift
74 and Vannucchi, 2004; Huene and Scholl, 1991). Trench sediment accumulates by surface
75 erosion of the continental crust and resembles average upper continental crust (Plank,
76 2004; Plank and Langmuir, 1993). Eroded crust is continental crust that is mechanically
77 removed by the subducting slab from forearc basement either by frontal or basal tectonic
78 erosion (Huene et al., 2004; Huene and Scholl, 1991).

79 Trench sediment recycling has been deduced by the strong compositional links
80 between arc magmas and conjugate trench sediments (e.g. Kay, 1980; Kelemen et al.,
81 2003; Morris et al., 2002; Morris et al., 1990; Plank, 2004; Plank and Langmuir, 1993), and
82 unequivocally confirmed by the detection of cosmogenic ^{10}Be in young arc lavas (Morris
83 et al., 2002; Tera et al., 1986). In contrast, subduction erosion was first recognized from
84 geological observations. For example, uplifted igneous plutonic roots of older arcs may
85 be exposed trenchward to modern arcs which suggests a landward retreat of the trench
86 and forearc crustal removal (Huene and Scholl, 1991; Schaaf et al., 1995). Missing crust is
87 also indicated by vertical fore-arc subsidence without horizontal extension or depression
88 (Huene and Scholl, 1991; Ranero and Huene, 2000). The intensity of subduction erosion
89 may vary considerably through time and among different arc-trench systems (Clift and
90 Vannucchi, 2004; Stern, 2011). On a global scale, mass balance calculations show that
91 subduction erosion accounts for about half (~44-50%) of the crust recycled in subduction
92 zones relative to the trench sediment (~42-56%) (Clift et al., 2009; Scholl and Huene,
93 2009). Regionally, eroded crust may even exceed the mass of trench sediment by up to a
94 factor of 10 (Vannucchi et al., 2003). Clearly, in view of these numbers, the recycled
95 eroded crust must leave a chemical imprint on the arc that rivals the influence of the
96 recycled trench sediment.

97 Confirming the recycling of eroded crust in the compositions of arc magmas,
98 however, is a major challenge. The eroded crust mingles with the incoming trench
99 sediment and subducted igneous oceanic basement (AOC, altered oceanic crust), and re-
100 emerges in volcanic arcs together with material from the mantle, and possibly
101 contaminated by the arc's crustal basement. These components must then be
102 distinguished from each other in arc magmas, whereby the eroded crust is similar to
103 trench sediment and arc basement. No unique tracer exists, such as ^{10}Be for oceanic

104 trench sediment. To add complexity, basal crust from the underside of the upper plate is
105 not accessible, which forestalls direct comparison to arc compositions. Nevertheless,
106 from comprehensive Sr-Nd-Pb-B isotope and trace element studies of arc magmas,
107 evidence for the presence of fore-arc eroded crust has begun to accumulate (e.g. Goss
108 and Kay, 2006; Goss et al., 2013; Holm et al., 2014; Kay et al., 2005; Risse et al., 2013;
109 Tonarini et al., 2011). The common factor of these studies is that they integrate geological
110 and geochemical observations that allow the detection of compositional mismatch
111 between arc chemistry and trench input from the subducted slab that may be reconciled
112 by crust removed from the fore-arc regions.

113 In the global spectrum of arc magmas, the Mexican margin is a prime setting for
114 tracing the eroded crust in volcanic arcs. First, there is strong evidence for long-term
115 crustal erosion along the Mexican Trench indicated by trench retreat and fore-arc uplift
116 (Clift and Vannucchi, 2004), and by large volumes of missing Mesozoic and Cenozoic
117 crust along the coast (Ducea et al., 2004; Keppie et al., 2012; Morán-Zenteno et al., 1996;
118 Schaaf et al., 1995). Second, the subducted crustal materials - trench sediment, AOC,
119 eroded crust – are obtainable from drill sites at the trench and offshore continental slope
120 as well as from coastal outcrops (exposed Acapulco intrusion, Hernández-Pineda et al.,
121 2011; Watkins and Moore, 1981). Since these crustal materials have distinct
122 compositions, they should be traceable in the arc magmas. Here we report the results of
123 comprehensive comparison between Sr-Nd-Pb-Hf-O-He isotope and trace element data
124 of olivine-bearing arc magmas from the central Mexican Volcanic Belt (MVB) and Sr-Nd-
125 Pb-Hf isotope and trace elements of relevant crustal input materials from the subducting
126 and overlying slab. Our data imply that crust recycled by subduction erosion controls
127 much of the chemistry of the arc magmas erupted in the central MVB.

128 2. GEOLOGICAL SETTING

129 The Mexican Volcanic Belt is an active Pliocene-Quaternary volcanic arc that is related
130 to the subduction of the Cocos and Rivera plates along the Middle American Trench
131 (Figure 1) (e.g. Gómez-Tuena et al., 2007b). The trench runs oblique to the arc volcanic
132 front at an angle of $\sim 17^\circ$, because the slab dip decreases eastward and the arc-trench gap
133 widens. In the central MVB, the slab subducts horizontally beneath the forearc and the
134 arc-trench gap measures ~ 360 km (Pardo and Suarez, 1995; Perez-Campos et al., 2008).
135 The study area in central Mexico comprises the monogenetic Sierra Chichinautzin
136 Volcanic Field that is flanked by the composite volcanoes Nevado de Toluca (west) and
137 Popocatepetl (east) (Figure 1, 2). The volcanoes are constructed on a ~ 45 km thick sialic
138 crust of Proterozoic granulites and Mesozoic metapelites, granites and limestones (e.g.

139 Ortega-Gutiérrez et al., 2012). An extensional crustal stress regime facilitates magma
140 ascent, and mafic and high-Mg# olivine-phyric basalts and andesites are common
141 (Gómez-Tuena et al., 2007b; Schaaf et al., 2005; Wallace and Carmichael, 1999).

142 Magma compositions in the central MVB range from basalt to dacites which display
143 considerable diversity in trace elements (e.g. Cai et al., 2014; LaGatta, 2003, and
144 references therein; Martinez-Serrano et al., 2004; Schaaf et al., 2005; Siebe et al., 2004a;
145 Straub et al., 2013a; Straub et al., 2014; Wallace and Carmichael, 1999). For petrogenetic
146 studies it was useful to distinguish between a 'basaltic' (olivine-normative) and
147 'andesitic' (quartz-normative) group, respectively (e.g. Straub et al., 2011b; 2013a; 2014).
148 For the discussion of recycling processes, however, we prefer a division based on the
149 source-sensitive incompatible trace elements (Figure 3). In trace element space, three
150 groups with basaltic and andesitic compositions can be distinguished (see also
151 Appendix A, Figure 1a). The first and far most abundant group (estimated >95 vol% of
152 erupted magmas) are calc-alkaline basalts to dacites (50-67 wt% SiO₂) which construct
153 the voluminous (several 100 km³) composite volcanoes and most of the small-volume (≤1
154 km³) monogenetic cones. Calc-alkaline magmas combine low Nb = 4-14 ppm
155 abundances with arc-typical strong enrichments of large-ion lithophile elements (LILE)
156 relative to the rare earth elements (REE) and high-field-strength elements (HFSE). The
157 second group ('high-La') consists of light REE (LREE)-enriched basalts to basaltic
158 andesites that have strongly fractionated trace element patterns with strong enrichments
159 in K₂O and LREE, relative depletions in Zr-Hf and steep heavy REE (HREE) patterns.
160 'High-La' magmas were first described by Gomez-Tuena et al. (2007a) in the Valle de
161 Bravo west of Nevado de Toluca. In the central MVB, only a few high-La magmas erupt
162 from small, monogenetic volcanoes but these magmas are more common in western
163 Mexico (Gomez-Tuena et al., 2011). The third group consists of Nb-rich (>17-36 ppm),
164 mildly alkaline basalts to basaltic andesites (49-57 wt% SiO₂). Nb-rich magmas are
165 enriched in LILE, REE and HFSE, and their trace element pattern resemble those of
166 enriched intraplate basalts (LaGatta, 2003; Schaaf et al., 2005; Straub et al., 2013a; Wallace
167 and Carmichael, 1999). Nb-rich magmas are ubiquitous in the rear-arc region of the
168 MVB, but are rare along the arc volcanic front (e.g. Díaz-Bravo et al., 2014; Gómez-Tuena
169 et al., 2007b; Luhr, 1997).

170 In the central MVB, Nb-rich magmas erupt from a small, likely coeval group (ca. 1600-
171 1800 year ago, Siebe, 2000; Siebe et al., 2004b; Straub et al., 2013b) of monogenetic
172 volcanoes in the center of the Sierra Chichinautzin, located halfway between
173 Popocatepetl and Nevada de Toluca (Figure 2) (e.g. Straub et al., 2013b; Wallace and

174 Carmichael, 1999). These Nb-rich magmas are closely associated with the calc-alkaline
175 magmas, erupting from vents only a few kilometers and a few thousands year apart,
176 and even from the same volcano (e.g. Suchiooc, Schaaf et al., 2005; Siebe et al., 2004a;
177 Straub et al., 2013a; Straub et al., 2014). In our sample set, the Nb-rich magmas are over-
178 represented, because they were the target of a more detailed study (Straub et al., 2013a,
179 2013b).

180 3. ARC MAGMA PETROGENESIS IN THE CENTRAL MVB

181 The impact of slab contributions (such as slab fluids, slab partial melts and more
182 recently 'slab diapirs', hereafter summarily referred to as 'slab components') on arc
183 magmas and its consequences for arc petrogenesis and subduction cycling are at the core
184 of arc research (e.g. Gomez-Tuena et al., 2014; Hacker et al., 2011; Plank, 2004). This
185 question is also intensely debated in the central MVB, where much recent progress was
186 made, and for which a short summary is provided here.

187 The central MVB is constructed on thick continental basement and consequently many
188 studies propose that andesites and dacites evolve from primary basaltic mantle melt by
189 crustal processing (fractional crystallization, crustal assimilation) (e.g. Agustín-Flores et
190 al., 2011; Marquez et al., 1999; Verma, 1999a). However, in recent years evidence has
191 accumulated from several comprehensive petrologic and geochemical studies that the
192 entire range of central MVB basaltic to andesitic (and even dacitic and rhyolitic) magmas
193 are near-primary melts from a subduction-modified mantle that pass the crustal
194 basement nearly unchanged (Gomez-Tuena et al., 2007a; Gómez-Tuena et al., 2008;
195 Straub et al., 2011a; Straub et al., 2013a; Straub et al., 2008). In these models high-Ni
196 olivines with up to 5400 ppm Ni play a key role (Appendix A, Figures 1b,c). These
197 olivines crystallize from basaltic and andesitic magmas and have high $^3\text{He}/^4\text{He}$ ratios of
198 7-8 R_a which confirms that their host magmas originate in upper mantle. Moreover, the
199 high Ni concentrations in olivine suggests that these magmas are partial melts of
200 secondary olivine-free pyroxenite segregations in the mantle wedge (Straub et al.,
201 2011b). Such segregations formed following the infiltration of silicic components from
202 slab. They melt preferentially relative to the surrounding peridotite in an upwelling
203 mantle and produce a broader range of primary basaltic to dacitic melts that mix
204 variably during ascent to form andesites (Straub et al., 2011a; Straub et al., 2013a; Straub
205 et al., 2008). A major implication of this 'pyroxenite model' is that the central MVB
206 magmas are principally mixtures of slab and mantle materials that underwent little, or
207 negligible, processing in the shallow crust. Thus, the budget of their highly incompatible

208 trace elements must be strongly controlled by recycled slab materials with little
209 influence of the subarc mantle.

210 This inference has to date been confirmed by follow-up studies which provided
211 additional insights (e.g. Straub et al., 2013a; 2014). First, the central MVB 'background
212 mantle' (mantle without subduction influence) is highly depleted through serial
213 ('repetitive') melting that is triggered by the continuous hydrous flux from slab since the
214 arc became active in Pliocene. Thus, the mantle wedge is very susceptible to be
215 chemically overprinted by slab additions (2013a; Straub et al., 2008; 2014). The effect of
216 only a few percent melt extraction on the pre-subduction mantle is illustrated in
217 Figure 3, by means of modeling the 'Old Texcal Flow'. This is a monogenetic basalt flow
218 that shows the least slab influence in central Mexico [e.g. lowest SiO₂ ~49 wt%, highest
219 TiO₂ ~2 wt% and lowest Ni in olivines that are only slightly higher than the Ni of
220 olivines in mid-ocean ridge basalts (MORB)], and is considered as best proxy to a melt
221 from the original mantle wedge (Straub et al., 2013a). In incompatible trace elements, the
222 'Old Texcal Flow' resembles a ~3-4% partial melt of the average primitive mantle (or
223 'pyrolite') as given by McDonough and Sun (1995) [see Straub (2013a)]. However, the
224 'Old Texcal Flow' has no end member character in trace element space (Figure 3). While
225 the 'Old Texcal Flow' is per definition a high-Nb basalt (Nb>17 ppm), it has the lowest
226 Nb abundances of this group (Nb=17-19 ppm) and is largely intermediate to calc-
227 alkaline and high-Nb series in other incompatible trace elements (Straub et al., 2014).
228 Therefore, primitive mantle cannot be the prevalent background mantle as it would
229 produce melts that are too enriched in HFSE and light REE for the calc-alkaline series.
230 However, a residual of primitive mantle, produced after only >3-10% melt loss, is highly
231 depleted incompatible elements, and can easily be modified by slab additions (Straub et
232 al., 2014). As discussed previously, in the central MVB, most of the incompatible trace
233 elements (including elements Sr, Nd, Pb and Hf which are associated with isotope
234 tracers) are either exclusively, or substantially contributed from the slab (Straub et al.,
235 2013a; 2014), excepting only Ti and HREE (Ho-Lu).

236 Second, regardless of the extent of depletion by melting, the Ti and HREE (Ho-Lu) are
237 always controlled by the mantle. In other words, calc-alkaline and high-Nb magmas
238 could contain larger amount of slab material without displaying a garnet signature.
239 Model calculations for REE that use the most recent partitioning data for fluid and/or
240 melt release from slab (Klimm et al., 2008; Skora and Blundy, 2010) show that absorption
241 of up to 30% of slab material would not increasing Ho/Lu of the metasomatized mantle
242 above MORB levels (Straub et al., 2013a; 2014). This amount agrees well with the

243 'pyroxenite model' that requires a minimum of 15-18% (and likely more) of a silicic slab
244 component in the source in order to convert peridotite to olivine-free pyroxenite (2011b;
245 Straub et al., 2008).

246 In summary, there is a confluence of evidence for strong slab contributions to the
247 mantle source that may make up several tens of percent of the erupted magmas (2014;
248 Gomez-Tuena et al., 2007a; Straub et al., 2011b; 2013a; 2014). At such proportions, the
249 slab components must control the highly incompatible trace element budgets of the
250 magmas. Moreover, slab components may range from strongly fractionated varieties to
251 components that equally mobilize fluid-mobile LILE, HFSE and LREE. Such diversity -
252 that likely represents heterogeneous slab material rather than an extreme range of
253 fractionation - would be ideal to produce the trace element diversity of calc-alkaline,
254 high-La and Nb-rich series that are so closely associated in time and space. Thus, the
255 central MVB magmas are not only suitable for more detailed investigations of the impact
256 of the slab flux on arc chemistry, but such studies are also a vital test of the prevailing
257 petrogenetic models.

258 4. SAMPLES AND DATA FOR THIS STUDY

259 Here we present new $\delta^{18}\text{O}$ data (n=51) for olivine phenocrysts, together with new Hf
260 and Pb isotope ratios of representative bulk rock samples (n= 37 samples). Most of these
261 samples have previously been analyzed for major and trace element abundances, Sr and
262 Nd isotope ratios, and the olivines have been analyzed for composition and $^3\text{He}/^4\text{He}$
263 (2011b; 2013a; Straub et al., 2008; 2014). In addition, 22 new volcanic rock samples were
264 analyzed for major and trace elements and Sr-Nd-Pb-Hf isotopes, as well as for major
265 element oxide and Ni concentrations of olivines of six samples (Appendix B Tables 1-5).
266 Furthermore, we analyzed up to 22 selected samples of crustal material (xenoliths,
267 basement) for major and trace elements and Sr-Nd-Pb-Hf isotope data (Appendix B
268 Tables 6-9) in order to complement the published data of crustal rocks from the
269 continental basement and offshore central Mexico (Figure 1). All new and previously
270 published data are summarized in Appendix B Table 10.

271 4.1. Central Mexican arc volcanic rocks

272 Sample locations for volcanic rocks are shown in Figure 2. Calc-alkaline samples are
273 from many monogenetic volcanoes and two composite volcanoes, Popocatepetl and
274 Toluca. The three high-La basalts and basaltic andesites are from monogenetic volcanoes
275 Yecahuazac Cone, Tuxtepec and St. Cruz. The Nb-rich series are from monogenetic
276 volcanoes Suchiooc, Chichinautzin and Texcal Flow.

277 **4.2. Crustal materials**

278 Crustal materials used in this study include (i) continental crustal basement on which
279 the MVB is constructed, (ii) coastal and offshore crustal basement, and (iii) the
280 terrigenous and pelagic sediment and AOC of the Cocos and Pacific plates (Figure 1).

281 **4.2.1. Continental crustal basement**

282 We obtained new Hf isotope data on crustal xenoliths from Chalcatzingo and Valle de
283 Santiago that have previously characterized for Sr-Nd-Pb isotopes and trace elements by
284 Gómez-Tuena et al. (2008, Chalcatzingo) and Ortega-Gutiérrez et al. (2014, Valle de
285 Santiago). Additional major and trace element data and Sr-Nd-Pb isotope ratios of
286 outcropping crust and crustal xenoliths from within and south of the Mexican Volcanic
287 Belt were compiled from Schaaf et al. (2005, Popocatepetl), Gomez-Tuena et al. (2003;
288 2008, Teziutlán (Puebla) and Chalcatzingo), Martinez-Serrano et al. (2004, Toluca),
289 Ortega-Gutiérrez et al. (2012; 2014, Puente Negro and Valle Santiago; 2011), and Pérez-
290 Gutiérrez et al. (2009, Xolapa terrane).

291 **4.2.2. Coastal and offshore continental crust**

292 We obtained coastal and offshore continental crust as proxies to crust recycled by
293 crustal erosion. The coastal samples are from the Eocene Acapulco intrusion that is now
294 exposed at the Pacific coast south of the central MVB (Hernández-Pineda et al., 2011).
295 Offshore samples are from DSDP Leg 66 drill sites that recovered biotite gneiss (Site 489)
296 and granodiorite (Site 493) basement southeast of Acapulco (Figure 1). We analyzed Hf
297 isotopes of the Acapulco intrusion [all other data are from Hernández-Pineda et al.
298 (2011)] and major and trace element abundances and Sr-Nd-Pb-Hf isotope ratios of the
299 DSDP basement samples (Appendix B Tables 7-9).

300 **4.2.3. Cocos and Pacific Plates**

301 The crustal compositions of the incoming Cocos Plate are either AOC or oceanic
302 sediment.

303 **4.2.3.1. Pelagic and terrigenous sediment**

304 There are two types of sediment subducted at the trench: (i) the pelagic sediment that
305 accumulated on the Cocos plate, and the (ii) terrigenous (hemipelagic) sediment from
306 the North American plate which covers the continental slope, trench and the near-trench
307 region of the Cocos plate (Watkins and Moore, 1981). The terrigenous sediment reaches
308 a minimum thickness of 625 m on the continental slope, and is still thicker (105 m) than
309 the pelagic sediment (65 m) at the trench Site 487 on the Cocos plate (Figure 1, Watkins
310 et al., 1981). Both sediment types were analyzed for major and trace element abundances

311 and Sr-Nd-Pb-Hf isotopes by Verma (1999b), LaGatta (2003) and Cai et al. (2014), mainly
312 with samples from DSDP Site 487 on the incoming Cocos plate, supplemented by
313 samples from DSDP Site 488 at the toe of the upper plate continental slope, and from
314 piston cores near the East Pacific Rise (Figure 1). A bulk trench sediment has been
315 calculated (Cai et al., 2014; Plank, 2014).

316 While not all data were obtained at each site, the two sediment types have clear
317 commonalities and differences. Both types have similar $^{143}\text{Nd}/^{144}\text{Nd}$ ~ 0.5125 and $^{87}\text{Sr}/^{86}\text{Sr}$
318 ~ 0.7085 , but the pelagic sediment has higher $^{176}\text{Hf}/^{177}\text{Hf}$ (~ 0.28294 vs. 0.28278) and Nd/Hf
319 (~ 20 vs 8) than the terrigenous sediment, and is less radiogenic in Pb isotopes (e.g.
320 $^{206}\text{Pb}/^{204}\text{Pb}$ 18.84 vs 18.52) (Cai et al., 2014; LaGatta, 2003). These differences allow these
321 two lithologies to be traced through the Mexican margin given the sensitivity of arcs
322 towards trench sediment (e.g. Carpentier et al., 2008; Elliott et al., 1997; Plank and
323 Langmuir, 1993).

324 4.2.3.2. Subducting igneous oceanic crust (AOC)

325 The subducted AOC has been characterized for trace elements and Sr-Nd-Pb-Hf
326 isotopes using the Miocene basalt basement drilled at DSDP Site 487 on the incoming
327 Cocos Plate (Cai et al., 2014; Verma, 1999b). These data and additional Sr-Nd-Pb-Hf
328 isotope analyses of two Site 487 basement samples (Appendix B Table 7) show that the
329 Site 487 basement resembles depleted zero-age mid-ocean ridge basalts of the East
330 Pacific Rise (PetDB, 2011). Nevertheless, the AOC now beneath the central MVB is about
331 ~ 5 - 6 million years older than at the trench, based on the current convergence rate of 47
332 km/Ma and the arc-trench gap of 360 km (e.g. Manea and Manea, 2011). In order to
333 preclude the possibility of a significant temporal change of the AOC, we analyzed 9
334 basaltic glasses spanning 10 - 72 Ma from the western flank of the East Pacific Rise
335 (Pacific Plate), assuming that the crust on both flanks of the East Pacific Rise represents
336 the upwelling mantle. Sample locations are shown in Figure 1 and include DSDP Sites
337 163 , 469 , 470 and 472 , ODP Sites 1217A , 1243B and IODP Sites 1332 , 1333 and 1334 . Sr-
338 Nd-Pb-Hf isotope ratios for all sites, and major element oxide abundances for three sites
339 are given in Appendix Tables 8 and 9. The trace element composition of these MORB
340 glasses are from Brandl et al. (2011; 2015).

341 5. ANALYTICAL METHODS

342 The majority of the Hf isotope ratios ($n=37$) were obtained at the Institute for Earth
343 Sciences (IES), Academia Sinica, Taipei, Taiwan on a Nu Plasma using the chemical Hf
344 separation technique after Lee et al. (1999). Additional Sr-Nd-Pb-Hf isotope ratios of

345 MVB lavas, crustal material and MORB glasses were obtained at Lamont using chemical
346 separation procedures developed by Cai et al. (2014). All trace element data of bulk
347 rocks were obtained by solution ICP-MS methods at the Centro de Geociencias (CGEO),
348 Juriquilla/Qro., Universidad Nacional Autónoma de México, Mexico. Major element
349 oxides were obtained by solution ICP-OES at Lamont. Oxygen isotope data of olivine
350 were obtained at the University of Oregon at Eugene. Olivine major and trace element
351 analyses and major element analyses of MORB glasses were performed at the American
352 Museum of Natural History in New York/USA. Details of analytical methods are given
353 in Appendix B together with the new data (Appendix B Tables 1-9).

354 6. RESULTS

355 6.1. O isotopes of the central MVB magmas

356 The $\delta^{18}\text{O}$ of olivines range from 5.3 to 6.6‰, which corresponds to $\delta^{18}\text{O}_{\text{melt}} = 6.3\text{--}8.4\text{‰}$
357 of their basaltic and andesite equilibrium melts (Figure 4) (fractionation-correction after,
358 Bindeman, 2008). The $\delta^{18}\text{O}_{\text{oliv}}$ extend to higher values than those reported by Johnson et
359 al. (2009) in young basalts from monogenetic volcanoes in the Michoacan-Guanajuato
360 Volcanic Field farther to the west ($\delta^{18}\text{O}_{\text{oliv}} = 5.5\text{--}6.0\text{‰}$). Together with the olivines of
361 Kluchevskoy volcano, Kamchatka which have $\delta^{18}\text{O}_{\text{oliv}}$ up to 7.6‰ (Auer et al., 2009),
362 central Mexico has the highest $\delta^{18}\text{O}_{\text{oliv}}$ reported in arc magmas worldwide (Martin et al.,
363 2011). Notably, the Nb-rich magmas have similar values and ranges in $\delta^{18}\text{O}_{\text{melt}}$ (=
364 $7.2 \pm 0.5\text{‰}$, $n=16$) as the calc-alkaline ($\delta^{18}\text{O}_{\text{melt}} = 7.4 \pm 0.5\text{‰}$, $n=24$) and high-La series
365 ($\delta^{18}\text{O}_{\text{melt}} = 6.6\text{--}7.3\text{‰}$, $n=2$). The olivines of the Old Texcal Flow ($\delta^{18}\text{O}_{\text{oliv}} = 5.6\text{‰}$), which
366 best approximates the mantle prior to subduction modification, have one of the lowest
367 melt $\delta^{18}\text{O}_{\text{melt}} = 6.4\text{‰}$ of the MVB. While still slightly above the range of MORB-type
368 mantle melts ($\delta^{18}\text{O}_{\text{melt}} = 5.7 \pm 0.2 \text{‰}$, Bindeman, 2008), the data confirm the end member
369 character of the Old Texcal Flow (Straub et al., 2013a).

370 6.2. Sr-Nd-Pb-Hf isotope ratios

371 The Sr-Nd-Pb-Hf isotope ratios of our samples are within the range reported from
372 previous studies (e.g. Cai et al., 2014; Martinez-Serrano et al., 2004; Meriggi et al., 2008;
373 Schaaf et al., 2005; Siebe et al., 2004a). Our data, however, illustrate for the first time the
374 systematic differences between calc-alkaline, high-La and Nb-rich magmas in all four
375 isotope systems (Figures 5-7). In Sr-Nd isotope space, the calc-alkaline and high-La
376 magmas are displaced to higher $^{87}\text{Sr}/^{86}\text{Sr}$ and/or higher $^{143}\text{Nd}/^{144}\text{Nd}$ relative to the Nb-
377 rich series (Figure 5). The Old Texcal Flow has the most radiogenic $^{143}\text{Nd}/^{144}\text{Nd}$ and least
378 radiogenic $^{87}\text{Sr}/^{86}\text{Sr}$ closest to Cenozoic MORB which agrees with its end member

379 character in trace element space (Straub et al., 2013a). In Nd-Hf isotope space, the calc-
380 alkaline and high-La series, and the Nb-rich magmas, respectively, define two parallel,
381 partially overlapping trends along the terrestrial array (Vervoort et al., 2011) (Figure 6)
382 with the calc-alkaline series being displaced towards higher $^{176}\text{Hf}/^{177}\text{Hf}$ at a given
383 $^{143}\text{Nd}/^{144}\text{Nd}$. Again, the Old Texcal Flow has the most radiogenic $^{143}\text{Nd}/^{144}\text{Nd}$ and
384 $^{176}\text{Hf}/^{177}\text{Hf}$ of the central MVB magmas, close in composition to Cenozoic MORB. In Pb
385 isotope space, all arc samples plot on a tight, linear array whereby the Nb-rich series
386 show a displacement towards more radiogenic Pb relative to the calc-alkaline magmas
387 (Figure 7) that is typical for the MVB (Díaz-Bravo et al., 2014; Gomez-Tuena et al.,
388 2007a). However, the Old Texcal Flow does not form the most radiogenic end member,
389 but plots in the middle of the arc array near the transition between calc-alkaline and
390 high-Nb series with a slight, but significant displacement toward higher $^{206}\text{Pb}/^{204}\text{Pb}$.

391 The Sr-Nd-Pb isotope range of the arc magmas is much more limited than that of the
392 crustal xenoliths which represent the crustal basement (Figure 5). The arc magmas
393 generally align better with potentially recycled crustal components, such trench
394 sediment, AOC, the Acapulco/offshore granodiorites and biotite gneiss which either
395 coincide or bracket the arc array. We note that the relationships between the arc magmas
396 and the recycled components differ in all four isotope systems. For example, in Sr-Nd
397 isotope space, arc magmas are bracketed by AOC and trench sediment, and overlap
398 with the Acapulco/offshore granodiorites, whereas the biotite gneiss is far more
399 enriched than any of these components. In Nd-Hf isotope space, however, the calc-
400 alkaline and high-La arc magmas are instead bracketed by the radiogenic AOC and the
401 unradiogenic granodiorites, respectively, while the trench sediments plots off the arc
402 trend. In this diagram, the Nb-rich magmas extend to slightly more unradiogenic Nd
403 and Hf isotopes than the granodiorites, and the biotite gneiss is far more unradiogenic
404 than any of these compositions. In Pb isotope space, the Cenozoic AOC and the pelagic
405 trench sediment are less radiogenic than the arc magmas, while terrigenous sediment,
406 granodiorites and biotite gneiss are more radiogenic. The granodiorite partially overlaps
407 with the high-Nb series, but not with the calc-alkaline magmas.

408 7. DISCUSSION

409 7.1. No evidence for crustal contamination

410 We emphasize that the new data in their entirety confirm the lack of shallow crustal
411 differentiation in the central MVB magmas (Straub et al., 2011b; 2013a; 2014). As
412 discussed earlier, and exemplified by $^{143}\text{Nd}/^{144}\text{Nd}$ in Figure 8a, the systematic increase of
413 melt silica with radiogenic isotope ratios rules out melt evolution by fractional

414 crystallization, but links the melt silica increase to changes in source composition
415 (Gomez-Tuena et al., 2007a; Straub et al., 2013a; Straub et al., 2014). Crustal assimilation
416 (or a combination of fractional crystallization and crustal contamination), which is often
417 invoked for such correlations, however, fails in view of the $^3\text{He}/^4\text{He}$ - $\delta^{18}\text{O}$ signature of
418 the high-Ni olivines in the basaltic to andesitic magmas (Figure 4).

419 The high-Ni, high $^3\text{He}/^4\text{He}$ =7-8 R_a olivines are either the only or first silicate phase in
420 all three magma series (calc-alkaline, high-La, and high-Nb magmas) (Schaaf et al., 2005;
421 Siebe et al., 2004a; Straub et al., 2008). As early-crystallizing olivines, they retain the
422 primary He-O isotopic signatures of the arc melts before possible later crustal
423 assimilation and secondary alteration (e.g. Eiler et al., 2000; Martelli et al., 2008). The
424 $^3\text{He}/^4\text{He}$ is extremely sensitive towards crustal assimilation, but the high $^3\text{He}/^4\text{He}$ of the
425 olivines does not correlate with melt SiO_2 , despite as little as 0.01% mass of assimilated
426 upper crust would be sufficient to lower the melt $^3\text{He}/^4\text{He}$ below the observed range
427 (Figure 8b). This argues against crustal contamination. On the other hand, the high
428 $\delta^{18}\text{O}_{\text{melt}}$ values of the olivines are clearly above mantle values regardless of the
429 fractionation correction, and point to a crustal component in the melts (Figure 8d,e).
430 While the olivine $\delta^{18}\text{O}$ does not correlate with the average olivine Fo_{78-90} (corresponding
431 to $\text{Mg}\#=53-74$ of melt) (Figure 9), it increases with increasing SiO_2 of the host melts
432 (Figure 8b). The increase exceeds the $\delta^{18}\text{O}$ increase predicted by fractional crystallization,
433 which agrees with results from high- $\delta^{18}\text{O}$ olivine studies in the western MVB (Johnson
434 et al., 2009). This correlation cannot be attributed to crustal assimilation either, as mixing
435 of a high-Mg#, low SiO_2 , low $\delta^{18}\text{O}$ component (e.g. basaltic mantle melt) with low-Mg#,
436 high SiO_2 , high $\delta^{18}\text{O}$ crustal component predicts correlation of the $\delta^{18}\text{O}$ with both melt
437 SiO_2 and Mg#. Moreover, several tens percent of crustal material would be required in
438 order to reproduce the increase in melt SiO_2 (Figure 8d), which exceeds by far any mass
439 tolerated by the $^3\text{He}/^4\text{He}$ of the olivines. Thus, if there is a crustal component in the
440 central MVB melts, it must have been added from slab. Recycled crustal material, such
441 as trench sediment or eroded crust, is initially rich in radiogenic ^4He and has a low
442 $^3\text{He}/^4\text{He} < 0.1$ (e.g., Martelli et al., 2008), but this He is driven off thermally in the
443 subduction cycle. For one, the highest closure temperature for He in common rock
444 forming minerals is $T_c = 600^\circ\text{C}$ (Martelli et al., 2008). Therefore, subducted crustal ^4He is
445 unlikely to survive the prolonged subduction beneath the Mexican fore-arc, where the
446 slab slowly heats up $>600^\circ\text{C}$ before reaching ca. $700-900^\circ\text{C}$ at arc front depth (e.g. Ferrari
447 et al., 2012; Manea and Manea, 2011). To the other, any remaining crustal He is unlikely
448 to survive heating to temperatures $>700^\circ\text{C}$ during infiltration of the slab material into the
449 hot mantle wedge prior to melt formation.

450 In summary, there is no evidence of significant crustal contamination in the basaltic
451 and andesitic magmas at least in the olivine crystallization stage. Rather, the olivines
452 crystallize from basaltic to andesitic mantle melts that contain a crustal component from
453 the subducted slab. Remarkably, a correlation between melt silica and $\delta^{18}\text{O}$ is expected
454 from the 'pyroxenite model' of melt-rock reaction that predicts the melt SiO_2 abundance
455 of primary melts to increase with the amount of recycled slab component (e.g.
456 incompatible trace elements, $\delta^{18}\text{O}$) in the mantle source (Straub et al., 2011b; 2014). Here,
457 the melting of secondary pyroxenite veins can create melt series with compositional
458 characteristics reminiscent of fractional crystallization and/or crustal assimilation
459 despite of a different genesis (Straub et al., 2014).

460 7.2. Identifying recycled slab components in Sr-Nd-Pb-Hf isotope space

461 7.2.1. Constraints from Sr-Nd-Pb-Hf systematics

462 The $^3\text{He}/^4\text{He}$ - $\delta^{18}\text{O}$ data constrain the presence of a slab-derived crustal component in
463 the arc magmas, but they do not identify this component which could be AOC, trench
464 sediment or eroded crust, or a mixture of those. This information can be obtained
465 through comparison of arc input and output in Sr-Nd-Pb-Hf isotope and trace element
466 space. To date, studies proposed that the Sr-Nd-Pb-Hf isotope range of the MVB
467 magmas was a mixture of components from the subducted AOC and trench sediment,
468 and mantle wedge (e.g. Cai et al., 2014; Gomez-Tuena et al., 2007a; Straub et al., 2013a;
469 Straub et al., 2014). If this is correct, then mixing trends calculated with these end
470 members must pass through the arc data in Sr-Nd-Pb-Hf isotope space. We tested this
471 inference by calculating first-order mixing curves shown in Figures 5-7. The shape of
472 isotope mixing curves depends only on the isotope and element ratios of the end
473 members, but not the concentrations of the elements (Langmuir et al., 1978). Because
474 AOC (~MORB) and the mantle wedge have similar elemental and - in first
475 approximation - also isotopic ratios, binary mixing curves between AOC and trench
476 sediment are sufficient to test the validity of the AOC-trench sediment-mantle mixing
477 models prior to full quantification. Binary first-order mixing curves were calculated with
478 measured end members given in Table 2.

479 In Sr-Nd-Pb isotope space, the arc magmas plot on, or reasonably close to,
480 AOC/mantle - trench sediment mixing curves (Figures 5,7). In Pb isotope space, the
481 Cenozoic AOC (average $^{206}\text{Pb}/^{204}\text{Pb}$ ~18.1) is a better fit than the average of zero-age East
482 Pacific Rise MORB which is more radiogenic ($^{206}\text{Pb}/^{204}\text{Pb}$ ~18.4) (PetDB, 2011) (Figure 7).
483 Moreover, the granodiorite and biotite gneiss emerge as possible crustal end member on
484 Sr-Nd-Pb mixing curves, together with the trench sediment. The Sr-Nd-Pb isotopic ratios

485 do not distinguish between trench sediment and granodiorite/biotite gneiss crustal
486 components. However, this seems possible in Nd-Hf isotope space, because of the
487 different mixing trajectories between AOC/mantle, trench sediment and
488 granodiorite/biotite gneiss. Mixing curves between AOC/mantle, and trench sediment
489 are strongly curved, because these end members have very different Nd/Hf ratios
490 (trench sediment Nd/Hf ~8-20, AOC Nd/Hf ~4, mantle Nd/Hf ~4). Therefore, these
491 curves miss the arc magmas. However, the mixing curves between AOC/mantle and
492 granodiorite are nearly linear and pass through most of the arc data, as the granodiorite
493 and biotite gneiss have a similar low Nd/Hf ~5-7 as the AOC/mantle component. This is
494 confirmed in the corresponding $^{176}\text{Hf}/^{177}\text{Hf}$ vs Nd/Hf diagram, where mixing trends are
495 linear. Again, the mixing lines between AOC/mantle and trench sediment, and
496 particularly AOC/mantle - pelagic trench sediment, clearly miss the bulk of the arc data,
497 while the granodiorite emerges as ideal crustal end member for most of the calc-
498 alkaline/high-La arc magmas, excepting only the Nb-rich magmas which extend to less
499 radiogenic Hf ratios than the granodiorites.

500 The shape of the AOC-sediment Nd-Hf isotope mixing curves is affected by Nd/Hf
501 fractionation, which may happen during release from slab (e.g. Kessel et al., 2005).
502 Current experimental and observational data disagree on the direction of fractionation.
503 For example, some studies suggest that Nd is preferentially released in slab fluids
504 ($D_{\text{Nd}}/D_{\text{Hf}} < 1$) at pressures of 4 GPa or in a zircon-bearing slab (Kessel et al., 2005; Rubatto
505 and Hermann, 2003). On the other hand, an allanite-saturated slab may preferentially
506 retain Nd relative to Hf at 2.5 to 3 GPa ($D_{\text{Nd}}/D_{\text{Hf}} > 1$) (Klimm et al., 2008; Skora and
507 Blundy, 2010). Therefore, forward models are inconclusive, and we used an inverse
508 approach to test for the possible influence of Nd/Hf fractionation. This is done by
509 varying the Nd/Hf of trench sediment or AOC in a three component mixture (mantle,
510 AOC, sediment) until the Nd-Hf isotope mixing curve passed through the arc data. In
511 short, partial curve fits can be achieved in Nd-Hf isotope space by decreasing the Nd/Hf
512 of the trench sediment or increasing the Nd/Hf of the AOC by a factor of 7 (which is
513 high). However, both solutions fail in the corresponding Nd/Hf vs $^{176}\text{Hf}/^{177}\text{Hf}$ array.
514 Decreasing Nd/Hf of the trench sediment causes the corresponding mixing curves to
515 pass below the arc data in the Nd/Hf vs $^{176}\text{Hf}/^{177}\text{Hf}$ diagram (Figure 10a,b). Increasing
516 Nd/Hf of the AOC, result the corresponding mixing curve plots above the bulk of arc
517 data (Figure 10b,c). The only exception is the high-La group that it could be fit if one of
518 the slab components had a high, fractionated Nd/Hf.

519 In summary, the Nd-Hf trace element and isotope systematics strongly argue for the
520 granodiorite/biotite gneiss eroded from the forearc as crustal end member in the arc
521 magmas instead of the trench sediment. The granodiorite appears the volumetrically
522 more important recycled lithology, as it seems prevalent in the ubiquitous calc-alkaline
523 series. In contrast, the biotite gneiss is much farther removed from the arc array, and fits
524 lesser well with the arc trends than the granodiorite.

525 7.2.2. *Other slab components and processes*

526 While the high-La and Nb-rich series are close to the calc-alkaline magmas in isotope
527 space, their trace element characteristics require additional processes and/or source
528 components. The calc-alkaline and high-La series likely involve the same source
529 materials, but the much higher Nd/Hf of the high-La series (by up to a factor of 3) points
530 to fractionation of these elements which most likely occurs during release from slab. The
531 few high-La magmas do not form trends in Nd-Hf isotope and trace element space and
532 thus provide no clue as which slab component - AOC or granodiorite, or a mixture of
533 both - fractionates. The fractionated nature of this slab component is consistent with
534 their other characteristics, such as the low Nb (=4-8 ppm) which is coupled with high
535 Nb/Ta (17.2-19.5) and LREE-enrichment. Arc magmas with similar signatures are
536 globally rare, but have been reported from the western MVB (Gomez-Tuena et al., 2011)
537 and the Solomon and Indonesia arcs (Goss and Kay, 2009; Koenig and Schuth, 2011;
538 Stolz et al., 1996). In either setting, these magmas have been linked to deep (≥ 140 km)
539 partial melting of an fairly hot (>900 - 1050°C) eclogitic slab that has residual rutile, but
540 lost all other REE-bearing phases like monazite and allanite (Gomez-Tuena et al., 2011;
541 Koenig and Schuth, 2011). Deep partial slab melts that escaped mingling with other slab
542 component released at shallower depths could account for the isolated eruption of high-
543 La in randomly distributed small ($\ll 1$ km²) cones remote from composite and larger
544 monogenetic volcanoes.

545 The Nb-rich magmas contain isotopically different source components, as evident
546 from their systematic differences to the calc-alkaline/high-La magmas in Sr-Nd-Pb-Hf
547 space (Figures 10-12). The similarity of the Nb-rich magmas to intraplate magmas has
548 lead to suggestions that these may derive from inherently enriched mantle domains (Cai
549 et al., 2014; Gomez-Tuena et al., 2011; Wallace and Carmichael, 1999). However, their
550 high $\delta^{18}\text{O}$ and high-Ni olivines as well as details of major and trace element systematics
551 (Straub et al., 2013a) clearly point to a slab influence that is comparable in magnitude to
552 that of calc-alkaline series in most of the Nb-rich magmas. Thus, the isotopic differences
553 imply that the mantle sources of the Nb-rich magmas were infiltrated by isotopically

554 different slab components(s). More than one factor, however, is responsible for the
555 isotopic differences. One factor is that the calc-alkaline/high-La series are more hydrous
556 than the Nb-rich series, having several wt% melt water compared to ≤ 1 wt% of the Nb-
557 rich magmas (e.g. Cervantes and Wallace, 2003a; Johnson et al., 2009; Roberge et al.,
558 2009). Thus, and consistent with previous models (e.g. Gomez-Tuena et al., 2007a; Straub
559 et al., 2014), the source of the calc-alkaline/high-La series seems to receive more slab
560 fluids, such as Sr- and Pb -rich fluids (or possibly hydrous melts) from AOC. An AOC
561 fluid rich in the unradiogenic Pb of the Cenozoic MORB-type crust may shift the calc-
562 alkaline/high-La magmas towards lesser radiogenic Pb isotope ratios relative to the
563 high-Nb magmas in Pb isotope space (Figure 12). AOC fluids may also carry Sr with a
564 $^{87}\text{Sr}/^{86}\text{Sr}$ higher (up to ~ 0.705 , Staudigel et al., 1995) than that fresh MORB ($^{87}\text{Sr}/^{86}\text{Sr} \sim 0.702$ -
565 3) of AOC, and shift the calc-alkaline/high-La magmas towards higher $^{87}\text{Sr}/^{86}\text{Sr}$ at a given
566 $^{143}\text{Nd}/^{144}\text{Nd}$ (Figure 11) (e.g. Gomez-Tuena et al., 2007a; 2013a; Straub et al., 2014).

567 A fractionated fluid component that is enriched in fluid mobile LILE relative to the
568 HFSE does not account for the trace element budget of the Nb-rich magmas. Instead, the
569 slab component infiltrating the source of the Nb-rich magmas must be rich in Nb and
570 Ta, and have high Nb/Ta (16-19.4), high Nb/La (~ 0.9), low Th/La (0.11) and the low
571 Nd/Hf (~ 4). This rules out the granodiorites or similar crustal material as source as this
572 material has fractionated trace element signatures which it would transmit to the mantle
573 (Appendix Figure 2). On the other hand, intraplate basalts have the requisite isotope and
574 trace signatures (e.g. Hofmann, 2003). We tentatively suggest that the source of the high-
575 Nb magmas may have been infiltrated by crust constructed by intraplate seamount
576 magmas. It is possible that such seamount crust was part of the largely inaccessible
577 continental fore-arc basement. Alternatively, it could be part of subducting Cocos plate
578 where clusters of intraplate seamounts are common (e.g. Bohrson and Reid, 1995;
579 Castillo et al., 2010; Niu and Batiza, 1997). Local recycling of seamount material,
580 mingling to some extent with granodiorite, could account for the limited distribution of
581 the Nb-rich magmas in space and time in the Sierra Chichinautzin (Straub et al., 2013b)
582 as well as along the volcanic front of the entire MVB.

583 **7.3. Magnitude and impact of the eroded crust on arc magmas**

584 The granodiorite emerges are important component in the arc magmas. In order to
585 quantitatively assess its influence, we used a combination of inverse methods (trace
586 elements) and forward modeling techniques (radiogenic isotopes). This two-fold
587 approach minimizes the inherent uncertainties of flux quantification where many
588 variables are model-dependent.

589 **7.3.1. Estimating the total slab flux from trace elements**

590 First, we estimated the total percentage of slab-derived Sr, Pb, Nd and Hf in the arc
591 magmas by the inverse method of Pearce et al. (1995a). The method calculates the
592 difference for each sample between the observed concentration of an element – which is
593 that of a melt from the subduction-modified mantle - and its concentration in a
594 hypothetical melt from the same mantle free from slab additions ('background mantle').
595 These differences then scale to the percentage of the slab-derived element in the arc
596 magmas. Assuming Nb and Yb to be mantle-derived, Pearce et al. (1995a) used Nb/Yb
597 ratios to calculate the 'background magma'. In the central MVB, however, Nb is added
598 from slab, and hence TiO_2/Lu is used (Straub et al., 2013a; 2014). Moreover, instead of
599 MORB-type mantle source (Pearce et al., 1995a), we used primitive mantle for
600 calculating the slab-derived percentages for the high-Nb magmas, and residual
601 primitive mantle (after 3.5% melt extraction) calculating those of the calc-alkaline and
602 high-La magmas. Only with magmas with $\text{Mg}\# > 60$ were used in order to ensure the use
603 of trace element ratios in the most primitive magmas.

604 The trace element inversion confirms a strong slab flux of Sr, Nd, Pb and Hf for all
605 three arc magma series, with the Nb-rich magmas (>44-59% of Sr, Nd, Pb and Hf slab-
606 derived) having about one third less slab contribution than the calc-alkaline (>69-89%)
607 and high-La series (73-96%) (Table 1). In Figure 13, the slab-derived percentages are
608 plotted against the relevant isotopic composition. The Old Texcal Flow is always the
609 least influenced by the slab flux (slab-derived Pb ~18%, Sr ~34% Nd ~16% Hf ~20%) and
610 forms a common point of origin from which the trends of calc-alkaline/high-La and
611 high-Nb magmas diverge towards different slab components. These trends agree with a
612 model of a homogenous mantle that was infiltrated by at least two isotopically distinct
613 slab components. Remarkably, there are no clear trends towards the trench sediment,
614 which confirms its negligible influence on the arc magmas. This is most evident for the
615 arc Sr that must principally originate from recycled AOC and/or granodiorite, without
616 any apparent contribution of sedimentary Sr. Another feature is that none of the arc
617 trends heads towards the same, or the same mix, of slab components in all four isotope
618 systems. This supports the concept of the slab flux being a composite of several
619 individual components that mix in variable proportions.

620 **7.3.2. Quantifying the slab sources in isotope space**

621 Forward mixing models in isotope space allow for the estimation of the individual
622 contributions of mantle and slab components to the arc magmas. The first step is to fit
623 mixing curves through the arc data with the appropriate end members (mantle, AOC,

624 granodiorite/seamounts). A model curve is valid if (i) it passes through the data, and (ii)
625 the modeled elemental ratios reasonably reproduce those of the magmas. We first used
626 the measured elemental ratios of the end members (Table 2). If the mixing curve did not
627 pass through the arc data, then the elemental ratios of the slab-derived end members
628 were modified based on the results from experimental studies.

629 Suitable mixing curves can be generated in Nd-Hf-Pb isotope space without problem
630 (Figures 10,12). In Sr-Nd isotope space, however, the Sr/Nd of the slab component needs
631 to be adjusted in order to reproduce the high Sr/Nd of the arc magmas (calc-
632 alkaline/high-La series Sr/Nd~25±4; Nb-rich magmas Sr/Nd ~19±4). This exceeds those of
633 the main sources (mantle ~12-16, AOC ~12, granodiorite ~9, intraplate seamounts ~13).
634 Mixing curves were fitted by increasing the AOC Sr by a factor of 2.5 for the Nb-rich
635 magmas. For the calc-alkaline series, the Sr flux was increased by a factor of 3 for
636 granodiorite and 4 for AOC. While these adjustments are somewhat arbitrary, they
637 provide a measure of the magnitude of the required Sr excess from slab. The final
638 isotope and elemental ratios of the end members are given in Table 2.

639 For the calculation of the Sr-Nd-Pb-Hf mixing curves, compositions of idealized,
640 average end member are used (Figures 10-12). While mantle, AOC and granodiorite
641 compositions are reasonably well known (Table 2), the composition of the inferred
642 recycled seamount component is unknown, and therefore its quantification is tentative.
643 For an estimate, we used the Sr, Nd, Pb and Hf abundances of off-axis seamounts with
644 Nb >13-46 ppm from Niu and Batiza (1997), and estimated the isotope ratios of end
645 members from the Sr-Nd-Pb-Hf isotope mixing systematics of the arc magmas.

646 Two different types of background mantle were chosen: a primitive mantle for the
647 Nb-rich magmas, and a residuum of primitive mantle after 3.5% melt extraction for the
648 calc-alkaline and high-La series (Table 2). The elemental abundances and ratios of the
649 slab components vary considerably depending on whether the slab material is released
650 as bulk component ('slab diapir'), or as partial fluid or melt. Forward estimates are thus
651 inherently uncertain because these depend on a multitude of often poorly known
652 variables (e.g. metamorphic history of slab, partition coefficients, mixing proportions,
653 slab residual mineralogy, thermal structure and composition, physical properties).
654 Again, we choose the simplest approach by using the measured elemental abundances
655 of the end members, with only the abundance adjustment for Sr (Table 2). This approach
656 minimizes the calculated influence of the slab flux on the arc magmas. In addition,
657 mixing proportions were chosen to minimize the contributions of granodiorite. In Sr-
658 Nd-Hf isotope space, the arc data can be reproduced with a slab component composed

659 of 50% AOC and 50% granodiorites (or seamount material for the high-Nb magmas).
660 The same mixing ratio is valid for the AOC-seamount slab component in Pb isotope
661 space. The granodiorites, however, are so enriched in Pb relative to mantle and AOC
662 that only 10% in the slab component is needed to reproduce the data. A 20% of the
663 composite slab component was mixed with the mantle wedge, which is consistent with
664 major and trace element constrained from previous studies (Straub et al., 2011b; 2013a;
665 2014). Modeling parameters are given in Table 2, and the results are summarized in
666 Table 3.

667 In summary, the isotope models suggest (within model uncertainty) a slab flux similar
668 in magnitude to results to that produced by the trace element inversion with the
669 exception of Hf (Tables 1 and 3). Slab-derived percentages are for Sr ~78-96% (compared
670 to 49-95% from trace element inversion), for Pb ~76-86% (59-96% from inversion), for Nd
671 ~76-87% (47-93% from inversion) and for Hf ~75-87% (44-73% from inversion). The
672 significant observation is the high slab contribution relative to that of the mantle wedge,
673 and in particular that of the granodiorite. The granodiorite controls the isotope
674 chemistry of the calc-alkaline magmas/high-La, to which they supply most of the Sr
675 ~73%, Pb ~61%, Nd ~68% and Hf ~87%. Likewise, the purported seamount component
676 makes a strong, but somewhat lesser contribution to the Nb-rich magmas (Sr ~37%, Pb
677 ~54%, Nd ~51% and Hf ~46%) relative to mantle and AOC. The overall contributions of
678 the AOC fluids to the arc magmas are fairly low, with only Sr ~23-42%, Pb ~22-25%, Nd
679 ~21-25% and Hf ~27-28%. Even if contribution of the Pb AOC is likely underestimated,
680 as the model makes no allowance for Pb enrichment in AOC fluids, the moderate
681 influence of AOC-derived Pb on the arc Pb isotope ratios agrees with their lack of
682 isotopic overlap with AOC, which is unlike many other arcs where the influence of AOC
683 components is much stronger (Figures 11, 12) (e.g. Straub and Zellmer, 2012). Overall,
684 the modeling results imply a strong influence of eroded granodiorite on the calc-alkaline
685 and high-La magmas, while the Nb-rich magmas are influenced to similar extent by
686 another slab component (possibly seamounts).

687 **7.4. Why does the trench sediment align with the MVB magmas in Sr-Nd-Pb** 688 **isotope space?**

689 The Acapulco/offshore granodiorites, possibly complemented by an unknown
690 seamount component, provide an excellent recycled crustal component for the MVB
691 magmas, but the question remains why the trench sediments align so well with the arc
692 magmas in Sr-Nd-Pb isotope space? A simple answer may be that trench sediment and
693 arc magmas are essentially mixtures of the same, or similar, components from

694 continental crust and MORB. The arc magmas, however, form by mixing of these
695 components in the mantle, whereas the sediments form by mixing on the Earth' surface.
696 Marine sediment is essentially the debris of continental erosion (lithogenic dust, volcanic
697 ash, riverine and hemipelagic input) that is diluted by biogenic components in the
698 oceans (Plank, 2004; Plank and Langmuir, 1998; Vervoort et al., 2011). The sediment
699 $^{87}\text{Sr}/^{86}\text{Sr}$ and $^{143}\text{Nd}/^{144}\text{Nd}$ is controlled by Nd- and Sr-rich debris and dust from the North
700 American continent, and is similar in pelagic and terrigenous sediments. The continental
701 debris also controls the Pb isotope composition of the sediments, but close to mid-ocean
702 ridges the continental signal is overprinted by MORB-type Pb delivered by
703 hydrothermal fluids. Thus, only the terrigenous sediment (Pb = 21 ppm) reflects the Pb
704 isotopes of the continental crust, whereas the Pb-rich pelagic sediment (Pb= 66 ppm
705 LaGatta, 2003) is displaced towards the unradiogenic Pb typical of Cenozoic MORB. In
706 Nd-Hf isotope and trace element space, however, sediment does not align with crust-
707 mantle trends, because of fractionation during transport from the continent. For
708 example, early loss of Hf-rich heavy minerals in rivers (e.g. zircon) increases the Nd/Hf
709 ratio of the suspended load, and hydrothermal fluids may change the Nd and Hf isotope
710 ratios of the continental debris (e.g. Garçon et al., 2013; Garçon et al., 2014; Vervoort et
711 al., 2011). Thus, the Nd-Hf isotope and trace element signature of the continental crust is
712 different from the trench sediment, allowing their signatures to be discriminated in the
713 arc magmas.

714 **7.5. Recycling by slab diapirism – a physical model**

715 **7.5.1. Estimating the amount of eroded recycled crust**

716 A significant outcome of our study is that the trench sediment does not influence the
717 central MVB arc magmas. However, there is no evidence for sediment accumulation in
718 the trench, and all trench sediment seems to have been subducted (Manea et al., 2003).
719 Consequently, the signal of the trench sediment in the calc-alkaline arc magmas must be
720 concealed by the eroded granodiorite. We estimated the minimum amount of
721 granodiorite needed to conceal the trench sediment from the Nd and Hf fluxes. The
722 volume of the trench sediment is $\sim 8.84 \text{ km}^3/\text{km}/\text{Myr}$, at a convergence rate of 52
723 km/Myr, thickness of 170 m (Plank, 2014), density of $1370 \text{ kg}/\text{m}^3$ and water content of 59
724 wt%. Thus, it supplies Nd= $169.3 \text{ g}/\text{km}/\text{Myr}$ and Hf= $10.6 \text{ g}/\text{km}/\text{Myr}$ with an average
725 Nd/Hf =16 [based on Plank (2014)]. A similar thickness of granodiorite with a density of
726 $2700 \text{ kg}/\text{m}^3$ and zero water content would supply Nd= $782.9 \text{ g}/\text{km}/\text{Myr}$ and Hf= 136.0
727 $\text{g}/\text{km}/\text{Myr}$ with an average Nd/Hf=5.8. Therefore, in order to generate Nd/Hf <6 of the
728 total recycled crustal component, the mass of eroded crust must exceed that of the trench

729 sediment by at least 9-10 times. This corresponds to a minimum rate of recycled
730 granodiorite of ~79-88.4 km³/Myr.

731 This estimate exceeds by more than two times the estimate of Ducea et al. (2004) who
732 inferred one-dimensional exhumation rates of 0.18 km/Myr from (U-Th)/He
733 thermochronology of the south central Mexican basement, and estimated ~30
734 km³/km/Myr crustal loss by subduction during the Miocene. On the other hand, our
735 estimate compares well with the numbers derived from the reconstruction of the shape
736 of the missing Eocene to Miocene fore-arc. The unusual location of the MVB at ~360 km
737 from the trench has been interpreted as the result of a process of slab flattening between
738 middle and late Miocene (Ferrari et al., 1999). Thus, the pre-Miocene arc location is
739 inferred from the configuration of the general Rivera-Cocos subduction, where the arc is
740 ~150 km from the trench in the Jalisco-Colima region, but between 150 and 200 km from
741 the trench in Guatemala. At fore-arc crustal thickness of 20 km (Kim et al., 2010), the
742 crustal loss would be between 20x150km²=3000 km² and 20x200 km²=4000km². Given the
743 ~50 Ma age of batholiths of the Acapulco coast (Hernández-Pineda et al., 2011), and a
744 ~17 Ma start of the MVB volcanic activity (Gómez-Tuena et al., 2007b), this yields an
745 average rate of 60-80 km³/km/Myr for the last in 50 Ma. Thus, our estimate can be
746 considered as realistic.

747 **7.5.2. Granodiorite recycling by slab diapirism**

748 The high rate of recycled granodiorite has consequences for the style of mass transfer
749 from slab to wedge. Assuming the subducted granodiorite to be ~9-10 times thicker than
750 trench sediment (= 170 m thick), it would reach a thickness of ~1500-1700 meters.
751 Together with the typical low density of a quartz-feldspar lithology (2700 kg/m³) and the
752 estimated slab temperatures below the arc front of ~700-900°C (Ferrari et al., 2012;
753 Manea and Manea, 2011), these are ideal conditions for buoyant detachment of the
754 granodiorite from slab as 'slab diapirs' without need for slab melting (Behn et al., 2011;
755 Gerya et al., 2004; Gómez-Tuena et al., 2014; Hacker et al., 2011). Such slab diapirs are a
756 highly efficient way to transfer large amounts of slab material into the mantle wedge.
757 Silicic diapirs can react with the peridotite in similar ways as perceived for silicic slab
758 fluids or melts, and form secondary pyroxenites. Importantly, as the granodiorite has
759 similar low average Ho/Lu = 2.5 ± 0.5 as the mantle wedge (Ho/Lu ~2.2), it will not
760 impose a garnet signature on the mantle either.

761 A recycling cartoon is shown in Figure 14. The granodiorite is depicted to rise
762 buoyantly in the form of diapirs without melting. It may have little intrinsic water, but
763 water could be added from the dewatering AOC, as well as from serpentinite lithologies

764 from within and below the AOC (e.g. Gómez-Tuena et al., 2014). The granodiorite
765 diapirs dominate by far the slab flux, and are complemented by deep slab melts may
766 form at >140 km and infiltrate the source of the high-La magmas. The high-Nb magmas
767 are tentatively interpreted to be recycled intraplate seamount crust that is entrained into
768 the granodiorite diapirs. All slab components rise into the hot interior of the mantle
769 wedge where they react with the peridotite to form pyroxenite segregations that then
770 melt in the upwelling mantle, and mix during ascent through mantle and crust. The
771 numerous, closely spaced, but compositionally highly diverse small volume
772 monogenetic volcanoes ($\leq 1 \text{ km}^3$) may be the surface expressions of a heterogeneous sub-
773 arc mantle interspersed with pyroxenite veins. On the other hand, a succession of
774 individual slab diapirs channelized at a preferred spot of over a longer period of time
775 (several 100 ka to 1 million years), may ultimately accumulate the eruptive volumes of
776 several 100 km^3 typical of the composite volcanoes (e.g. Gómez-Tuena et al., 2014).

777 **7.6. The impact of subduction erosion on the central MVB magmas**

778 Our recycling model implies that the slab flux controls the budget of the highly
779 incompatible elements in the arc magmas. We tested this inference by means of the
780 incompatible element ratios Th/La and Nb/Ta, that are difficult to fractionate during
781 subduction processing (e.g. Foley et al., 2002; Plank, 2004). Th/La ratios (≈ 0.09 to 0.37)
782 span the global range from the low Th/La (~ 0.05) of the mantle to the high Th/La (~ 0.37)
783 of upper continental crust (e.g. Plank, 2004; Rudnick and Gao, 2002). The range of Nb/Ta
784 (≈ 12.3 -19.5) is similarly broad, and only excludes the rare, superchondritic Nb/Ta >19.9
785 reported from some arcs (Gomez-Tuena et al., 2011; Koenig and Schuth, 2011; Stolz et al.,
786 1996) (Figure 15).

787 Mixing relationships with $^{143}\text{Nd}/^{144}\text{Nd}$ confirm that the Th/La and Nb/Ta of the calc-
788 alkaline series is inherited from the inherently heterogeneous granodiorite. The
789 granodiorites form a perfect end member that would buffers the MVB magmas at high
790 $^{143}\text{Nd}/^{144}\text{Nd}$ and at a broader range of Th/La and Nb/Ta. Some granodiorites also have
791 the low Th/La and high Nb/Ta intrinsic to the high-Nb magmas. However, oceanic
792 seamounts have the same characteristics and provide a more likely end member given
793 their isotopic and trace element composition (Figure 15).

794 The strong influence of the various recycled components on MVB melt chemistry is
795 best evident in Nb vs Nb/Ta space (Figure 16). The Old Texcal Flow (proxy to melt from
796 mantle wedge prior to subduction modification) divides this diagram into four
797 quadrants. The high-La magmas all plot in the upper left quadrant which combines high
798 Nb/Ta >17 with low Nb concentrations typical of a signature of deep melts from eclogitic

799 slabs with residual rutile (Gomez-Tuena et al., 2011; Koenig and Schuth, 2011). The high-
800 Nb series occupy quadrant II with their combination of high Nb and Nb/Ta being
801 tentatively attributed to the recycling of seamount material. The calc-alkaline magmas
802 (quadrant III), have the low Nb and Nb/Ta (~12-16) typical of continental crust material,
803 here recycled by subduction erosion. Calc-alkaline magmas with these characteristics
804 dominate the entire MVB volcanic front (2014; Gómez-Tuena et al., 2007b). Previous
805 studies linked the low arc Nb/Ta to the partial melting of an amphibole-bearing slab, as
806 amphibole is the only major slab phase that can retain Nb relative to Ta, and produces
807 slab melts with low Nb and Nb/Ta (Foley et al., 2002; Gomez-Tuena et al., 2007a; Gomez-
808 Tuena et al., 2011; Koenig and Schuth, 2011). However, most of the MVB arc front is
809 located >80 km above the slab and thus beyond the amphibole-eclogite transition
810 (Tatsumi and Eggins, 1995). Here, regardless of amphibole stability, recycling of pre-
811 existing continental crust with intrinsically low-Nb/Ta provides a simpler cause for the
812 predominantly low Nb/Ta of MVB magmas.

813 Likewise, if the granodiorite transmits the high Th/La to the calc-alkaline series, there
814 is no need for additional Th/La fractionation of the magmas, either during slab
815 processing (e.g. Cai et al., 2014) or by shallow crustal differentiation (e.g. Plank, 2004).
816 Additional Th/La fractionation is only needed if all source components had lower Th/La
817 than the arc. While AOC, mantle wedge and average trench sediment all have low Th/La
818 (Cai et al., 2014), the granodiorite (Th/La=0.25±0.10) has similar high and variable Th/La
819 as the calc-alkaline arc magmas (=0.21±0.06). Here, our results support the crustal
820 recycling model of Plank (2004) who proposed that the high Th/La in global arcs is
821 essentially inherited from perpetual recycling of continental crust via the trench
822 sediment (~upper continental crust, Plank and Langmuir, 1998) and expand it to include
823 continental crust recycled by subduction erosion.

824 There are other compositional features that the calc-alkaline central MVB may inherit
825 from granodiorite. The low Sr/Y ~11 of the granodiorite, regardless of additional Sr from
826 AOC fluids, appears to control the low Sr/Y of the arc magmas (<50). This explains the
827 absence of 'adakitic' high Sr/Y > 50 in the central MVB that has been considered as arc
828 with a 'young and hot' slab prone to melting in previous studies (e.g. Cai et al., 2014;
829 Defant and Drummond, 1990). The granodiorites may also buffer the Ba, Rb, Ba and Pb
830 abundances on the arc to their comparatively low abundances, which are too low if the
831 arc input would be made up AOC and the trench sediment that is highly enriched in
832 these elements (Gomez-Tuena et al., 2007a). Overall, the central MVB poses an excellent
833 example for a volcanic arc that may principally grow by recycling of pre-existing

834 continental crust rather than through the creation of new arc crust by subduction
835 processing.

836 8. CONCLUSIONS

837 The following are the conclusions of this study:

- 838 (1) The Nd-Hf isotope and trace element systematics of central Mexican arc magmas
839 identify granodiorites eroded from the continental fore-arc, and not trench
840 sediment, as the principal recycled component of continental crust.
- 841 (2) The calc-alkaline arc magmas of the central MVB (>95% of the erupted volume) are
842 mixtures of recycled granodiorite, subducted AOC and mantle wedge. Rare,
843 strongly fractionated high-La magmas, and a minor group of Nb-rich magmas, can
844 be linked to deep slab melting, and the local recycled of seamount material,
845 respectively.
- 846 (3) With an estimated mass flux of 79-88 km³/km/Myr, thickness of 1500-1700 m and
847 density of 2700 kg/m³, the eroded granodiorite layer is conducive to the buoyant
848 ascent from slab in form of 'slab diapirs', with no need for slab melting, at the
849 estimated slab temperatures of 700-900°C.
- 850 (4) Th/La, Nb/Ta and other key trace element ratios of the calc-alkaline magmas are
851 inherited from the granodiorite, suggesting that the MVB arc grows by recycling of
852 the continental crust rather than by formation of new continental crust.

853

854 9. ACKNOWLEDGEMENTS

855 Special thanks to Der-Chuen Lee, Wen-Yu Hsu and Kuo-Lung Wang for help with Hf
856 separation and isotope analysis at the Institute of Earth Sciences at Academia Sinica
857 (Taipei/Taiwan), and to Ofelia Pérez-Arvizu for help with isotope and trace element
858 analyses at Lamont and the UNAM Centro de Geociencias/Queretaro, Mexico, and to
859 Charlie Langmuir, Terry Plank and Catherine Chauvel for discussion. Vincente Loreto
860 Becerra, Jesús Valenzuela González, Hermes Samir Herrera Fernández and Sergio Nuño
861 Licona provided valuable support in the field. Yue Cai is thanked for help with isotope
862 separation procedures at Lamont. Catherine Chen, Ellen Knapp, Rose Ramirez and
863 Maggie Sochko assisted with sample preparation. Four anonymous reviewers and
864 Associate Editor Andreas Stracke are thanked for their constructive comments. The
865 IODP Gulf Coast Repository/TX provided the samples from DSDP Leg 66 and IODP
866 Legs 320/321. Support from National Science Foundation grants EAR-07-38707 and EAR-

867 12-20481, and from National Science Council of Taiwan grants 96-2811-M-001-023 and
868 98-2811-M-001-052 is gratefully acknowledged.

869

870 10. REFERENCES CITED

- 871 Agustín-Flores, J., Siebe, C., Guilbaud, M.N., 2011. Geology and geochemistry of Pelagatos, Cerro
872 del Agua, and Dos Cerros monogenetic volcanoes in the Sierra Chichinautzin Volcanic Field,
873 south of México City. *J Volcanol Geotherm Res* 201 143-162,
874 doi:110.1016/j.jvolgeores.2010.1008.1010.
- 875 Auer, A., Bindeman, I.N., Wallace, P.J., Ponomareva, V., Portnyagin, M., 2009. The origin of
876 hydrous, high- $\delta^{18}\text{O}$ voluminous volcanism: diverse oxygen isotope values and high magmatic
877 water contents within the volcanic record of Klyuchevskoy volcano, Kamchatka, Russia
878 *Contrib Mineral Petrol* 157.
- 879 Behn, M.D., Kelemen, P.B., Hirth, G., Hacker, B.R., Massonne, H.J., 2011. Diapirs as the source of
880 the sediment signature in arc lavas. *Nat Geoscience* 4, doi: 10.1038/NGEO1214.
- 881 Bindeman, I., 2008. Oxygen Isotopes in Mantle and Crustal Magmas as revealed by Single Crystal
882 analysis. *Rev Mineral Geochem* 69, 445-478, doi: 410.2138/rmg.2008.2169.2112.
- 883 Blatter, D.L., Carmichael, I.S.E., Deino, A.L., Renne, P.R., 2001. Neogene volcanism at the front of
884 the central Mexican volcanic belt: basaltic andesites to dacites, with contemporaneous
885 shoshonites and high-TiO₂ lavas. *Geol Soc Am Bull* 113, 1324-1342.
- 886 Bohrsen, W.A., Reid, M.R., 1995. Petrogenesis of alkaline basalts from Socorro Island, Mexico:
887 Trace element evidence for contamination of ocean island basalt in the shallow ocean crust *J*
888 *Geophys Res* 100, 24555-24576.
- 889 Brandl, P.A., Regelous, M., Beier, C., Haase, K.M., 2011. Chemical Evolution of the Oceanic Crust
890 on 103 - 108 Year Timescales, AGU Fall Meeting, San Francisco, pp. T31A-2327.
- 891 Brandl, P.A., Regelous, M., Beier, C., O'Neill, S.C., O, N., Haase, K.M., 2015. The chemical
892 stratigraphy of the extrusive oceanic crust: timescales of magma evolution at mid-ocean
893 ridges. submitted to *Lithos*.
- 894 Cai, Y., 2009. Tracing Upper Mantle Heterogeneities with radiogenic isotopes at the Mexican
895 Volcanic Belt and the Arctic Gakkel Ridge, Graduate School of Art and Philosophy. Columbia
896 University, New York, p. 243p.
- 897 Cai, Y., LaGatta, A., Goldstein, S.L., Langmuir, C.H., Gomez-Tuena, A., Martin del Pozzo, A.L.,
898 Carrasco-Nunez, G., 2014. Hafnium isotope evidence for slab melt contributions in hot slab
899 arcs: an example of the Central Mexican Volcanic Belt. *Chem Geol* 377, 45-55,
900 <http://dx.doi.org/10.1016/j.chemgeo.2014.1004.1002>.
- 901 Carpentier, M., Chauvel, C., Mattielli, N., 2008. Pb-Nd isotopic constraints on sedimentary input
902 into the Lesser Antilles arc system. *Earth Planet Sci Lett* 272, 199-211,
903 doi:110.1016/j.epsl.2008.1004.1036.
- 904 Castillo, P.R., Clague, D.A., Davis, A.S., Lonsdale, P.F., 2010. Petrogenesis of Davidson Seamount
905 lavas and its implications for fossil spreading center and intraplate magmatism in the eastern
906 Pacific. *G-cubed* 11, doi: 10.1029/2009GC002992.
- 907 Cervantes, P., Wallace, P.J., 2003a. The role of H₂O in subduction zone magmatism: New insights
908 from melt inclusions in high-Mg basalts from central Mexico. *Geochim Cosmochim Acta* 31,
909 235-238.

910 Clift, P.D., Vannucchi, P., 2004. Controls on Tectonic Accretion versus Erosion in Subduction
911 Zones: Implications for the Origin and Recycling of the Continental Crust *Reviews of*
912 *Geophysics* 42, RG2001, DOI: 2010.1029/2003RG000127.

913 Clift, P.D., Vannucchi, P., Morgan, J.P., 2009. Crustal redistribution, crust–mantle recycling and
914 Phanerozoic evolution of the continental crust. *Earth-Science Reviews* 97, 80-104,
915 doi:110.1016/j.earscirev.2009.1010.1003.

916 Defant, M., Drummond, M., 1990. Derivation of some modern arc magmas by melting of young
917 subducted lithosphere. *Nature* 347, 662-665.

918 Díaz-Bravo, B.A., Gómez-Tuena, A., Ortega-Obregón, C., Pérez-Arvizu, O., 2014. The origin of
919 intraplate magmatism in the western Trans-Mexican Volcanic Belt. *Geosphere* 10, 340–373,
920 doi:10.1130/GES00976.

921 Donnelly, K., Goldstein, S.L., Langmuir, C.H., Spiegelman, M., 2004. Origin of Enriched Ocean
922 Ridge Basalt and Implications for Mantle Dynamics. *Earth Planet Sci Lett* 226, 347-366.

923 Ducea, M.N., Valencia, V.A., Shoemaker, S., Reiners, P.W., DeCelles, P.G., Fernanda Campa, M.,
924 Moran-Zenteno, D., Ruiz, J., 2004. Rates of sediment recycling beneath the Acapulco trench:
925 Constraints from (U-Th)/He thermochronology. *J Geophys Res* 109, B09404,
926 doi:09410.01029/02004JB003112.

927 Eiler, J.M., Crawford, A., Elliott, T., Farelly, m.K.A., Valley, J.W., Stolper, E.M., 2000. Oxygen
928 isotope composition of oceanic-arc lavas. *J Petrol* 41, 229-256.

929 Elliott, T., Plank, T., Zindler, A., White, W., Bourdon, B., 1997. Element transport from subducted
930 slab to juvenile crust at the Mariana arc. *J Geophys Res* 102, 14991-15019.

931 Farley, K.A., Neroda, E., 1998. Noble gases in the Earth’s mantle. *Annu Rev Earth Planet Sci* 26,
932 189–218.

933 Ferrari, L., López-Martínez, M., Aguirre-Díaz, G., Carrasco-Núñez, G., 1999. Space-time patterns
934 of Cenozoic arc volcanism in central Mexico: From the Sierra Madre Occidental to the Mexican
935 Volcanic Belt. *Geochim Cosmochim Acta* 27, 303-306.

936 Ferrari, L., Orozco-Esquivel, M.T., Manea, V.C., Manea, M., 2012. The dynamic history of the
937 Trans-Mexican Volcanic Belt and the Mexico subduction zone. *Tectonophysics* 522-523, 122-
938 149, doi:110.1016/j.tecto.2011.1009.1018.

939 Foley, S.F., Tiepolo, M., Vannucci, P., 2002. Growth of early continental crust controlled by
940 melting of amphibolite in subduction zones. *Nature* 417, 837-840.

941 Garçon, M., Chauvel, C., France-Lanord, C., Huyghe, P., Lave, J., 2013. Continental sedimentary
942 processes decouple Nd and Hf isotopes. *Geochim Cosmochim Acta* 121, 177-195,
943 <http://dx.doi.org/110.1016/j.gca.2013.1007.1027>.

944 Garçon, M., Chauvel, C., France-Lanord, C., Limonta, M., Garzanti, E., 2014. Which minerals
945 control the Nd-Hf-Sr-Pb isotopic compositions of river sediments? *Chem Geol* 364, 42-55,
946 <http://dx.doi.org/10.1016/j.chemgeo.2013.1011.1018>.

947 GeoMapApp, 2014. Marine Geoscience Data System. <http://www.geomapapp.org/>.

948 Gerya, T.V., Yuen, D.A., Sevre, E.O.D., 2004. Dynamical causes for incipient magma chambers
949 above slabs. *Geochim Cosmochim Acta* 32, 89-92, doi:10.1130/G20018.20011.

950 Gómez-Tuena, A., Díaz-Bravo, B., Vázquez-Duarte, A., Pérez-Arvizu, O., Laura Mori, L., 2014.
951 Andesite petrogenesis by slab-derived plume pollution of a continental rift, in: Gomez-Tuena,
952 A., Straub, S.M., Zellmer, G.F. (Eds.), *Orogenic Andesite and Crustal Growth*. Geological
953 Society of London Special Publication, London, pp. 65-101, doi 110.1144/SP1385.1144.

954 Gomez-Tuena, A., LaGatta, A., Langmuir, C.H., Goldstein, S.L., Ortega-Gutiérrez, F., Carrasco-
955 Nunez, G., 2003. Temporal control of subduction magmatism in the eastern Trans-Mexican
956 Volcanic Belt: Mantle sources, slab contributions, and crustal contamination. *Geochem*
957 *Geophys Geosys* 8, 8913, doi:8910.1029/2002GC000421.

958 Gomez-Tuena, A., Langmuir, C.H., Goldstein, S.L., Straub, S.M., Ortega-Gutierrez, F., 2007a.
959 Geochemical Evidence for Slab Melting in the Trans-Mexican Volcanic Belt. *J Petrol* 48, 537-
960 562, doi:510.1093/petrology/egl1071.

961 Gomez-Tuena, A., Laura Mori, L., Goldstein, S.L., Perez-Arvizu, O., 2011. Magmatic diversity of
962 western Mexico as a function of metamorphic transformations in the subducted oceanic plate.
963 *Geochim Cosmochim Acta* 75 213-241, doi:210.1016/j.gca.2010.1009.1029.

964 Gómez-Tuena, A., Mori, L., Rincón-Herrera, N.E., Ortega-Gutiérrez, F., Solé, J., Iriondo, A., 2008.
965 The origin of a primitive trondhjemite from the Trans-Mexican Volcanic Belt and its
966 implications for the construction of a modern continental arc. *Geochim Cosmochim Acta* 36,
967 471–474, doi: 410.1130/G24687A.

968 Gómez-Tuena, A., Orozco-Esquivel, M.T., Ferrari, L., 2007b. Igneous petrogenesis of the Trans-
969 Mexican Volcanic Belt, in: Alaniz-Álvarez, S.A., Nieto-Samaniego, Á.F. (Eds.), *Geology of*
970 *México: Celebrating the Centenary of the Geological Society of México: Geological Society of*
971 *America Special Paper.*

972 Gomez-Tuena, A., Straub, S.M., Zellmer, G.F., 2014. An introduction to orogenic andesites and
973 crustal growth in: Gomez-Tuena, A., Straub, S.M., Zellmer, G.F. (Eds.), *Orogenic andesites*
974 *and crustal growth Geological Society of London, London, pp. 1-13, doi:10.1144/SP1385.1116*

975 Goss, A.R., Kay, S.M., 2006. Steep REE patterns and enriched Pb isotopes in southern Central
976 American arc magmas: Evidence for forearc subduction erosion? *Geochem Geophys Geosys* 7,
977 Q05016, doi:05010.01029/02005GC001163.

978 Goss, A.R., Kay, S.M., 2009. Extreme high field strength element (HFSE) depletion and near-
979 chondritic Nb/Ta ratios in Central Andean adakite-like lavas (~28°S, ~68°W). *Earth Planet Sci*
980 *Lett* 279, 97–109.

981 Goss, A.R., Mahlburg Kay, S., Mpodozis, C., 2013. Andean adakite-like high-Mg andesites on the
982 Northern margin of the Chilean-Pampean flat-slab (27-28°S) associated with frontal arc
983 migration and fore-arc subduction erosion. *J Petrol* 54, 2193-2234,
984 doi:2110.1093/petrology/egt2044.

985 Hacker, B.R., Kelemen, P.B., Behn, M.D., 2011. Differentiation of the continental crust by
986 reamination. *Earth Planet Sci Lett* 307 501-516, doi:510.1016/j.epsl.2011.1005.1024.

987 Harrison, M.T., 2009. The Hadean Crust: Evidence from >4 Ga Zircons. *Annu Re. Earth Planet Sci*
988 37, 479-505, doi:410.1146/annurev.earth.031208.100151.

989 Hernández-Pineda, G.A., Solari, L.A., Gómez-Tuena, A., Méndez-Cárdenas, D.L., Pérez-Arvizu,
990 O., 2011. Petrogenesis and thermobarometry of the ~50 Ma rapakivi granite-syenite Acapulco
991 intrusive: Implications for post-Laramide magmatism in southern Mexico. *Geosphere* 7, 1-20,
992 doi:10.1130/GES00744.00741.

993 Hofmann, A.W., 2003. Sampling Mantle Heterogeneity through Oceanic Basalts: Isotopes and
994 Trace Elements, in: Holland, H.D., Turekian, K.K., Carlson, R.W. (Eds.), *Treatise on*
995 *Geochemistry.* Elsevier, pp. 61-101, ISBN 100-108-043751-043756.

996 Holm, P.M., Søger, N., Thorup Dyhr, C., Rohde Nielsen, M., 2014. Enrichments of the mantle
997 sources beneath the Southern Volcanic Zone (Andes) by fluids and melts derived from
998 abraded upper continental crust. *Contrib Mineral Petrol* 167, 1004, DOI 1010.1007/s00410-
999 00014-01004-00418.

1000 Huene, R.v., Ranero, C.R., Vannucchi, P., 2004. Generic model of subduction erosion. *Geochim*
1001 *Cosmochim Acta* 32, 913-916, doi: 910.1130/G20563.20561.

1002 Huene, R.v., Scholl, D.W., 1991. Observations at convergent margins concerning sediment
1003 subduction, subduction erosion, and the growth of continental crust. *Reviews of Geophysics*
1004 29, 279-316.

1005 Jarosewich, E., Nelen, N., Norberg, J., 1980. Reference samples for electron microprobe analysis.
1006 Geostandard Newsletter 4 (1), 43-47.

1007 Johnson, E.R., Wallace, P.J., Delgado-Granados, H., Manea, V.C., Kent, A.J.R., Bindeman, I.N.,
1008 Donegan, C.S., 2009. Subduction-related volatile recycling and magma generation beneath
1009 central Mexico: insights from melt inclusions, oxygen isotopes and geodynamic models. *J*
1010 *Petrol* 50, 1729-1764, doi:1710.1093/petrology/egp1051.

1011 Kay, R.W., 1980. Volcanic arc magmas: Implications of a melting-mixing model for element
1012 recycling in the crust-upper mantle system. *Journal of Geology* 88, 497-522.

1013 Kay, S.M., Godoy, E., Kurtz, A., 2005. Episodic arc migration, crustal thickening, subduction
1014 erosion, and magmatism in the south-central Andes. *Geol Soc Am Bull* 117, 67-88; doi:
1015 10.1130/B25431.25431.

1016 Kelemen, P.B., Yogodzinski, G., Scholl, D.W., 2003. Along-strike Variation in the Aleutian Island
1017 Arc: Genesis of high-mg# andesite and implication for the continental crust, in: Eiler, J. (Ed.),
1018 *Inside the Subduction Factory*. Amer Geophys Un, pp. 223-276.

1019 Keppie, D.F., Hynes, A.J., Lee, J.K.W., Norman, M., 2012. Oligocene-Miocene back-thrusting in
1020 southern Mexico linked to the rapid subduction erosion of a large forearc block. *Tectonics* 31,
1021 TC2008, doi:2010.1029/2011TC002976.

1022 Kessel, R., Schmidt, M.W., Ulmer, P., Pettke, T., 2005. Trace element signature of subduction-zone
1023 fluids, melts and supercritical liquids at 120-180 km depth. *Nature* 437, 724-727,
1024 doi:710.1038/nature03971.

1025 Kim, Y., Clayton, R.W., Jackson, J.M., 2010. Geometry and seismic properties of the subducting
1026 Cocos plate in central Mexico. *J Geophys Res* 115, doi:10.1029/2009JB006942, 002010.

1027 Klimm, K., Blundy, J.D., Green, T.H., 2008. Trace element partitioning and accessory phase
1028 saturation during H₂O-saturated melting of basalt with implications for subduction zone
1029 chemical fluxes. *J Petrol* 49, 523-553, doi:510.1093/petrology/egn1001.

1030 Koenig, S., Schuth, S., 2011. Deep melting of old subducted oceanic crust recorded by
1031 superchondritic Nb/Ta in modern island arc lavas. *Earth Planet Sci Lett* 301, 265-274,
1032 doi:210.1016/j.epsl.2010.1011.1007.

1033 LaGatta, A.B., 2003. Arc magma genesis in the Eastern Mexican Volcanic Belt, Department of
1034 Earth and Environmental Sciences. Columbia University, New York, p. 329.

1035 Langmuir, C.H., Vocke, R.D.J., Hanson, G.N., Hart, S.R., 1978. A general mixing equation with
1036 applications to Icelandic basalts. *Earth Planet Sci Lett* 37, 380-392.

1037 Lee, D.C., Halliday, A.N., Hein, J.R., Burton, K.W., Christensen, J.N., Guenther, D., 1999.
1038 Hafnium Isotope Stratigraphy of Ferromanganese Crusts. *Science* 285, 1052-1054.

1039 Luhr, J.F., 1997. Extensional tectonics and the diverse primitive volcanic rocks in the western
1040 Mexican Volcanic Belt. *Can Mineral* 35, 473-500.

1041 Manea, M., Manea, V.C., Kostoglodov, V., 2003. Sediment fill in the middle American trench
1042 inferred from gravity anomalies. *Geofis Int* 42, 603-612.

1043 Manea, V.C., Manea, M., 2011. Flat-slab thermal structure and evolution beneath central Mexico.
1044 *Pure Appl Geophys* 168, 1475-1487, doi 1410.1007/s00024-00010-00207-00029.

1045 Marquez, A., Oyarzun, R., Doblaz, M., Verma, S.P., 1999. Alkalic (ocean-island basalt type) and
1046 calc-alkalic volcanism in the Mexican Volcanic Belt: a case for plume-related and propagating
1047 rifting in an active margin. *Geochim Cosmochim Acta* 27, 51-54.

1048 Martelli, M., Nuccio, P.M., Stuart, F.M., Di Liberto, V., Ellam, R.M., 2008. Constraints on mantle
1049 source and interactions from He-Sr isotope variation in Italian Plio-Quaternary volcanism.
1050 *Geochem Geophys Geosys* 9, Q02001, doi:02010.01029/02007GC001730.

1051 Martin, E., Bindeman, I., Grove, T.L., 2011. The origin of high-Mg magmas in Mt Shasta and
1052 Medicine Lake volcanoes, Cascade Arc (California): higher and lower than mantle oxygen

1053 isotope signatures attributed to current and past subduction. *Contrib Mineral Petrol* 162, 945-
1054 960, doi 910.1007/s00410-00011-00633-00414.

1055 Martínez-Serrano, R.G., Schaaf, P., Solids-Pichardo, G., Hernández-Bernal, M.S., Hernández-
1056 Trevino, T., Morales-Contreras, J.J., Macías, J.L., 2004. Sr, Nd and Pb isotope and geochemical
1057 data from the Quaternary Nevado the Toluca volcano, a source of recent adakite magmatism,
1058 and the Tenango Volcanic Field. *J Volcanol Geotherm Res* 138, 77-110.

1059 McDonough, W.F., Sun, S.S., 1995. The composition of the Earth. *Chem Geol* 120, 223-253.

1060 Meriggi, L., Macías, J.L., Tommasini, S., Capra, L., Conticelli, S., 2008. Heterogeneous magmas of
1061 the Quaternary Sierra Chichinautzin volcanic field (central Mexico): the role of an amphibole-
1062 bearing mantle and magmatic evolution processes. *Revista Mexicana de Ciencias Geológicas*
1063 25, 197-216.

1064 Morán-Zenteno, D.J., Corona-Chavez, P., Tolson, G., 1996. Uplift and subduction erosion in
1065 southwestern Mexico since the Oligocene: pluton geobarometry constraints. *Earth Planet Sci*
1066 *Lett* 141, 51-65, doi: 10.1016/0012-1821X(1996)00067-00062.

1067 Mori, L., Gómez-Tuena, A., Cai, Y.M., Goldstein, S.L., 2007. Effects of prolonged flat subduction
1068 on the Miocene magmatic record of the central Trans-Mexican Volcanic Belt. *Chem Geol* 244
1069 (3-4), 452-473.

1070 Morris, J.D., Gosse, J., Brachfeld, S., Tera, F., 2002. Cosmogenic Be-10 and the Solid Earth: Studies
1071 in Geomagnetism, Subduction Zone Processes, and Active Tectonics, in: Grew, E. (Ed.),
1072 *Reviews in Mineralogy*. Mineralogical Society of America, Washington, DC, pp. 207-270.

1073 Morris, J.D., Leeman, W.P., Tera, F., 1990. The subducted component in island arc lavas:
1074 constraints from Be isotopes and B-Be systematics. *Nature* 344, 31-36.

1075 Muenker, C., Pfaender, J.A., Weyer, S., Buechl, A., Kleine, T., Mezger, K., 2003. Evolution of
1076 Planetary Cores and the Earth-Moon System from Nb/Ta Systematics. *Science* 301, 84-87.

1077 Munker, C., Weyer, S., Scherer, E., Mezger, K., 2001. Separation of high field strength elements
1078 (Nb, Ta, Zr, Hf) and Lu from rock samples for MC-ICPMS measurements. *Geochem*
1079 *Geophys Geosys* 2, doi: 10.1029/2001GC000183.

1080 Niu, Y., Batiza, R., 1997. Trace element evidence from seamounts for recycled oceanic crust in the
1081 Eastern Pacific mantle. *Earth Planet Sci Lett* 148, 471-483.

1082 Nowell, G.M., Kempton, P.D., Noble, S.R., Fitton, J.G., Saunders, A.D., Mahoney, J.J., Taylor,
1083 R.N., 1998. High precision Hf isotope measurements of MORB and OIB by thermal ionisation
1084 mass spectrometry: insights into the depleted mantle. *Chem Geol* 149 (3-4), 211-233.

1085 O'Nions, R.K., Oxburgh, E.R., 1988. Helium, volatile fluxes and the development of continental
1086 crust. *Earth Planet Sci Lett* 90, 331-347.

1087 Ortega-Gutiérrez, F., Elías-Herrera, M., Gómez-Tuena, A., Mori, L., Reyes-Salas, M., Macías-
1088 Romo, C., Solari, L.A., 2012. Petrology of high-grade crustal xenoliths in the Chalcatzingo
1089 Miocene subvolcanic field, southern Mexico: buried basement of the Guerrero-Morelos
1090 platform and tectonostratigraphic implications. *Int Geology Review* 54, 1597-1634,
1091 <http://dx.doi.org/1510.1080/00206814.00202011.00649956>.

1092 Ortega-Gutiérrez, F., Gómez-Tuena, A., Elías-Herrera, M., Reyes-Salas, M., Macías-Romo, C.,
1093 2014. Petrology and geochemistry of the Valle de Santiago lower-crust xenoliths: Young
1094 tectonothermal processes beneath the central Trans-Mexican volcanic belt. *Lithosphere* in
1095 press, doi: 10.1130/L1317.1131.

1096 Ortega-Gutiérrez, F., Martiny, B.M., Morán-Zenteno, D.J., Reyes-Salas, A.M., Solé-Viñas, J., 2011.
1097 Petrology of very high temperature crustal xenoliths in the Puente Negro intrusion: a
1098 sapphire-spinel-bearing Oligocene andesite, Mixteco terrane, southern Mexico. *Revista*
1099 *Mexicana de Ciencias Geológicas* 28, 593-629.

1100 Pardo, M., Suarez, G., 1995. Shape of the subducted Rivera and Cocos plate in southern Mexico:
1101 seismic and tectonic implications. *J Geophys Res* 100, 12357-12373.

1102 Pearce, J.A., Baker, P.E., Harvey, P.K., Luff, I.W., 1995a. Geochemical evidence for subduction
1103 fluxes, mantle melting and fractional crystallization beneath the South Sandwich Island Arc. *J*
1104 *Petrol* 36, 1073-1109.

1105 Perez-Campos, X., Kim, Y.H., Husker, A., Davis, P.M., Clayton, R.W., Iglesias, A., Pacheco, J.F.,
1106 Singh, S.K., Manea, V.C., Gurnis, M., 2008. Horizontal subduction and truncation of the Cocos
1107 Plate beneath central Mexico. *Geophys Res Lett* 35, 18303, doi:18310.11029/12008GL035127.

1108 Pérez-Gutiérrez, R., Solari, L.A., Gómez-Tuena, A., Martens, U., 2009. Mesozoic geologic
1109 evolution of the Xolapa migmatitic complex north of Acapulco, southern Mexico: implications
1110 for paleogeographic reconstructions. *Revista Mexicana de Ciencias Geológicas* 26, 201-221.

1111 PetDB, 2011. Information System for Geochemical Data of Igneous and Metamorphic Rocks from
1112 the Ocean Floor. <http://www.earthchem.org/petdb>.

1113 Pfänder, J.A., Münker, C., Stracke, A., Mezger, K., 2007. Nb/Ta and Zr/Hf in ocean island basalts -
1114 Implications for crust-mantle differentiation and the fate of Niobium. *Earth Planet Sci Lett*
1115 254, 158-172, doi:110.1016/j.epsl.2006.1011.1027.

1116 Pin, C., Briot, D., Bassin, C., Poitrasson, F., 1994. Concomitant separation of strontium and
1117 samarium-neodymium for isotopic analysis in silicate samples, based on specific extraction
1118 chromatography. *Analytica Chimica Acta* 298, 209-217.

1119 Plank, T., 2004. Constraints from Thorium/Lanthanum on Sediment Recycling at Subduction
1120 Zones and the Evolution of the Continents. *J Petrol* doi:10.1093/petrology/egi005, 1-24.

1121 Plank, T., 2014. The Chemical Composition of Subducting Sediments, in: Holland, H., Turekian,
1122 K. (Eds.), *Treatise on Geochemistry (Second Edition)*. Elsevier, pp. 607-629.

1123 Plank, T., Langmuir, C.H., 1993. Tracing trace elements from sediment input to volcanic output at
1124 subduction zones. *Nature* 362, 739-743.

1125 Plank, T., Langmuir, C.H., 1998. The geochemical composition of subducting sediment and its
1126 consequences for the crust and the mantle. *Chem Geol* 145, 325-394.

1127 Ranero, C.R., Huene, R.v., 2000. Subduction erosion along the Middle American convergent
1128 margin. *Nature* 404, 748-752.

1129 Risse, A., Trumbull, R.B., Kay, S.M., Coira, B., Romer, R.L., 2013. Multi-stage Evolution of Late
1130 Neogene Mantle-derived Magmas from the Central Andes Back-arc in the Southern Puna
1131 Plateau of Argentina. *J Petrol* 10, 1963-1995, doi:1910.1093/petrology/egt1038.

1132 Roberge, J., Delgado-Granados, H., Wallace, P.J., 2009. Mafic magma recharge supplies high CO₂
1133 and SO₂ gas fluxes from Popocatepetl volcano, Mexico. *Geochim Cosmochim Acta* 73, 107-
1134 110; doi: 110.1130/G25242A.

1135 Rubatto, D., Hermann, J., 2003. Zircon formation during fluid circulation in eclogites (Monviso,
1136 Western Alps): Implications for Zr and Hf budget in subduction zones. *Geochim Cosmochim*
1137 *Acta* 67, 2173-2187, doi:2110.1016/S0016-7037(2102)01321-01322.

1138 Rudnick, R., 1995. Making continental crust. *Nature* 378, 571-578.

1139 Rudnick, R., Gao, S., 2002. Composition of the Continental Crust, in: Rudnick, R.L. (Ed.), *The*
1140 *Crust*. Elsevier-Pergamon, Oxford, pp. 1-64.

1141 Schaaf, P., Morales-Zenteno, D., del Sol Hernandez-Bernal, M., Solis-Pichardo, G., Tolson, G.,
1142 Koehler, H., 1995. Paleogene continental margin truncation in southwestern Mexico:
1143 Geochronological evidence. *Tectonics* 14, 1339-1350.

1144 Schaaf, P., Stimac, J., Siebe, C., Macias, J.L., 2005. Geochemical evidence for mantle origin and
1145 crustal processes in volcanic rocks from Popocatepetl and surrounding monogenetic
1146 volcanoes, central Mexico. *J Petrol* 46, 1243-1282.

1147 Scholl, D.W., Huene, R.v., 2009. Implications of estimated magmatic additions and recycling
 1148 losses at the subduction zones of accretionary (non-collisional) and collisional (suturing)
 1149 orogens, in: Cawood, P.A., Kroener, A. (Eds.), *Earth Accretionary Systems in Space and Time*.
 1150 The Geological Society, Special Publications 2009, London, pp. 105-125, doi:
 1151 110.1144/SP1318.1144.
 1152 Siebe, C., 2000. Age and archaeological implications of Xitle volcano, southwestern Basin of
 1153 Mexico City. *J Volcanol Geotherm Res* 104, 45-64.
 1154 Siebe, C., Rodriguez-Lara, V., Schaaf, P., Abrams, M., 2004a. Geochemistry, Sr-Nd isotope
 1155 composition, and tectonic setting of Holocene Pelado, Guespalapa and Chichinautzin scoria
 1156 cones, south of Mexico City. *J Volcanol Geotherm Res* 130, 197-226.
 1157 Siebe, C., Rodriguez-Lara, V., Schaaf, P., Abrams, M., 2004b. Radiocarbon ages of Holocene
 1158 Pelado, Guespalapa, and Chichinautzin scoria cones, south of Mexico City: implications for
 1159 archeology and future hazards. *Bull Volcanol* 66, 203-225 DOI 210.1007/s00445-00003-00304-z.
 1160 Skora, S., Blundy, J., 2010. High-pressure hydrous phase relations of radiolarian clay and
 1161 implications for the involvement of subducted sediment in arc magmatism. *J Petrol* 51, 2211-
 1162 2243, doi:2210.1093/petrology/egq2054.
 1163 Staudigel, H., Davies, G.R., Hart, S.R., Marchant, K.M., Smith, B.M., 1995. Large scale isotopic Sr,
 1164 Nd and O isotopic anomaly of altered oceanic crust: DSDP/ODP sites 417/418. *Earth Planet Sci*
 1165 *Lett* 130, 169-185.
 1166 Stern, C.R., 2011. Subduction erosion: Rates, mechanisms, and its role in arc magmatism and the
 1167 evolution of the continental crust and mantle. *Gondwana Res* 20, 284-308,
 1168 doi:210.1016/j.gr.2011.1003.1006.
 1169 Stolz, A.J., Jochum, K.P., Spettel, B., Hofmann, A.W., 1996. Fluid- and melt-related enrichment in
 1170 the subarc mantle: Evidence from Nb/Ta variations in island-arc basalts. *Geochim Cosmochim*
 1171 *Acta* 24, 587-590.
 1172 Straub, S.M., Gomez-Tuena, A., Stuart, F.M., Zellmer, G.F., Cai, M.Y., Espinasa-Perena, R., 2011a.
 1173 High-Ni Olivines and the Mantle Origin of Arc Andesites, XXV IUGG General Assembly,
 1174 Melbourne, Australia.
 1175 Straub, S.M., Gomez-Tuena, A., Stuart, F.M., Zellmer, G.F., Espinasa-Perena, R., Cai, M.Y., Iizuka,
 1176 Y., 2011b. Formation of hybrid arc andesites beneath thick continental crust. *Earth Planet Sci*
 1177 *Lett* 303, 337-347, doi:310.1016/j.epsl.2011.1001.1013.
 1178 Straub, S.M., Gomez-Tuena, A., Zellmer, G.F., Espinasa-Perena, R., Stuart, F.M., Cai, Y.,
 1179 Langmuir, C.H., Martin-Del Pozzo, A., Mesko, G.T., 2013a. The processes of melt
 1180 differentiation in arc volcanic rocks: Insights from OIB-type arc magmas in the central
 1181 Mexican Volcanic Belt. *J Petrol* 54, 665-701, doi:610.1093/petrology/egs1081.
 1182 Straub, S.M., Gomez-Tuena, A., Zellmer, G.F., Espinasa-Perena, R., Stuart, F.M., Cai, Y.,
 1183 Langmuir, C.H., Martin-Del Pozzo, A., Mesko, G.T., 2013b. The processes of melt
 1184 differentiation in arc volcanic rock: Insights from OIB-type arc magmas in the central Mexican
 1185 Volcanic Belt: reply to a critical comment by Claus Siebe (2013). *J Petrol* 54, 1551-1554,
 1186 doi:1510.1093/petrology/egt1021
 1187 Straub, S.M., LaGatta, A.B., Martin-Del Pozzo, A.L., Langmuir, C.H., 2008. Evidence from high Ni
 1188 olivines for a hybridized peridotite/pyroxenite source for orogenic andesites from the central
 1189 Mexican Volcanic Belt. *Geochem Geophys Geosys* 9, Q03007, doi:03010.01029/02007GC001583.
 1190 Straub, S.M., Zellmer, G.F., 2012. Volcanic Arcs as Archives of Plate Tectonic Change. *Gondwana*
 1191 *Res* 21, 495-516, doi:410.1016/j.gr.2011.1010.1006
 1192 Straub, S.M., Zellmer, G.F., Gómez-Tuena, A., Espinasa-Perena, R., Martin-Del Pozzo, A.L.,
 1193 Stuart, F.M., Langmuir, C.H., 2014. A genetic link between silicic slab components and calc-
 1194 alkaline arc volcanism in central Mexico in: Gomez-Tuena, A., Straub, S.M., Zellmer, G.F.

1195 (Eds.), *Orogenic Andesites and Crustal Growth* Geological Society London Special
 1196 Publication, pp. 31-64, doi 10.1144/SP1385.1114.
 1197 Sun, S.S., McDonough, W.F., 1989. Chemical and isotopic systematics of oceanic basalts:
 1198 implications for mantle composition and processes, in: Saunders, A.D., Norry, M.J. (Eds.),
 1199 *Magmatism in the Ocean Basins*. Geol Soc Spec Publ Blackwell Scientific Publ, Oxford etc, pp.
 1200 313-345.
 1201 Tatsumi, Y., Eggins, E., 1995. *Subduction Zone Magmatism*. Blackwell Science, Cambridge MA.
 1202 Taylor, S.R., 1967. The origin and growth of continents. *Tectonophysics* 4, 17-34.
 1203 Tera, F., Brown, L., Morris, J., Sacks, I.S., 1986. Sediment incorporation in island-arc magmas:
 1204 Inferences from ¹⁰Be. *Geochim Cosmochim Acta* 50, 535-550.
 1205 Todt, W., Cliff, R.A., Hanser, A., Hofmann, A.W., 1996. Evaluation of a ²⁰²Pb-²⁰⁵Pb double-spike
 1206 for high-precision lead isotope analysis; in: Basu, A., Hart, S.R. (Eds.), *Earth Processes:
 1207 Reading the Isotopic Code*. AGU, Washington DC, pp. 429-437.
 1208 Tonarini, S., Leeman, W.P., Leat, P.T., 2011. Subduction erosion of forearc mantle wedge
 1209 implicated in the genesis of the South Sandwich Island (SSI) arc: Evidence from boron isotope
 1210 systematics. *Earth Planet Sci Lett* 301, 275–284, doi:210.1016/j.epsl.2010.1011.1008.
 1211 Vannucchi, P., Ranero, C.R., Galeotti, S., Straub, S.M., Scholl, D.W., McDougall-Ried, K., 2003.
 1212 Fast rates of subduction erosion along the Costa Rica Pacific margin: Implications for
 1213 nonsteady rates of crustal recycling at subduction zones. *J Geophys Res* 108, 2511,
 1214 2510.1029/2002JB002207.
 1215 Verma, S.P., 1999a. Geochemistry of evolved magmas and their relationship to subduction-
 1216 unrelated mafic volcanism at the volcanic front of the central Mexican Volcanic Belts. *J
 1217 Volcanol Geotherm Res* 93, 151-171.
 1218 Verma, S.P., 1999b. Geochemistry of the subducting Cocos plate and the origin of subduction-
 1219 unrelated mafic volcanism at the volcanic front of the central Mexican Volcanic Belt, in:
 1220 Delgado-Granados, H., Aguirre-Diaz, G., Stock, J.M. (Eds.), *Cenozoic Tectonics and Volcanism
 1221 at the volcanic front of the central Mexican Volcanic Belt*, pp. 1-28.
 1222 Vervoort, J.D., Plank, T., Prytulak, J., 2011. The Hf–Nd isotopic composition of marine sediments.
 1223 *Geochimica et Cosmochimica Acta* 75, 5903-5926, doi:5910.1016/j.gca.2011.5907.5046.
 1224 Wallace, P.J., Carmichael, I.S.E., 1999. Quaternary volcanism near the Valley of Mexico:
 1225 implications for subduction zone magmatism and the effects of crustal thickness variations on
 1226 primitive magma compositions. *Contrib Mineral Petrol* 135, 291-314.
 1227 Watkins, J.S., McMillen, K.J., Bachman, S.B., Shipley, T.H., Moore, J.C., Angevine, C., 1981.
 1228 Tectonic synthesis Leg 66: Transect and vicinity, in: Watkins, J.S., Moore, J.C. (Eds.), *DSDP Leg
 1229 66 Report*. US Gov Printing Office, Washington, pp. 837-849.
 1230 Watkins, J.S., Moore, J.C., 1981. Introduction: Scientific objectives and explanatory notes, Initial
 1231 Reports DSDP 66. US Govt Printing Office, Washington.
 1232

1233 11. **FIGURE CAPTIONS**

1234 Figure 1: Plate tectonic setting of the Trans-Mexican Volcanic Belt (MVB). **a.** Locations of
1235 DSDP/ODP/IODP drill sites samples on Pacific Plate (MORB glasses) and Cocos Plate (sediment,
1236 continental basement), and crust outcrops and xenoliths within and south of the MVB. Numbers
1237 in brackets next to IODP drill sites are basement ages in million years. Piston corer locations from
1238 Cai et al. (2014). Basemap from GeoMappApp (2014). **b.** Trans-Mexican Volcanic Belt (grey
1239 shaded) with principal Quaternary volcanoes redrawn from Blatter et al. (2001). Slab contours
1240 after Pardo and Suarez (1995). Locations of crustal materials are those of Gómez-Tuena et al.
1241 (2003, Palma Sola xenoliths), Martínez-Serrano et al. (2004, Nevado de Toluca xenoliths), Schaaf et
1242 al. (2005, Popocatepetl xenoliths), Gómez-Tuena et al. (2008, Chalcatzingo xenolith), Ortega-
1243 Gutiérrez et al. (2011, Puente Negro xenoliths), Hernández-Pineda et al. (2011, Eocene Acapulco
1244 intrusion), Pérez-Gutiérrez et al. (2009, Mesozoic Xolapa migmatites) and Ortega-Gutiérrez et al.
1245 (2014, Valle Santiago xenoliths). NDT – Nevado de Toluca, POP – Popocatepetl EPR – East
1246 Pacific Rise, RFZ – Rivera Fracture Zone, MC – Mexico City, TFZ – Tamayo Fracture Zone. **c.** NE-
1247 SW cross section of Mexican continental slope and trench with incoming Cocos plate drilled
1248 during DSDP Leg 66, redrawn from Watkins et al. (1981). Continental basement was drilled at
1249 Sites 493 (granodiorite) and 489 (B -biotite gneiss). Trench sediment was analyzed at Sites 488 and
1250 487 (Cai et al., 2014; LaGatta, 2003; Plank, 2014; Plank and Langmuir, 1998; Verma, 1999b), and
1251 oceanic basement at Site 487 (Cai et al., 2014, this study; Verma, 1999b).

1252

1253 Figure 2: Study area in the central Mexican Volcanic Belt. Monogenetic volcanoes (small open
1254 circles) of the Sierra Chichinautzin Volcanic Field are flanked by Quaternary composite volcanoes
1255 Nevado de Toluca and Popocatepetl-Iztaccihuatl. Large symbols denote samples with olivines
1256 analyzed for both $^3\text{He}/^4\text{He}$ and $\delta^{18}\text{O}$. Location of most mantle-like magmas ('Old Texcal Flow') is
1257 indicated, as well as location of high-La volcanic rocks (St. Cruz, Tuxtepec and Yecahuazac
1258 Cone). CV – City of Cuernavaca, TL City of Toluca

1259

1260

1261 Figure 3: Multi-element diagram of incompatible trace elements of central MVB magmas
1262 normalized to primitive mantle of McDonough and Sun (1995). For clarity, only magmas with
1263 high $^3\text{He}/^4\text{He}$ and high $\delta^{18}\text{O}$ are shown. **a.** Thick black line denotes the 'Old Texcal Flow' which is
1264 least influenced by slab and closely resembles a ~3.5% melt from primitive mantle (Straub et al.,
1265 2013a, 2013b). While per definition a high-Nb basalt (Nb=18 ppm), it has no end member
1266 character and is intermediate to calc-alkaline and high-Nb series. **b.** MVB magmas compared to
1267 melts from residual mantle after 3.5 to 10% melt extraction from a primitive mantle (which
1268 produced the Old Texcal Flow after minor subduction modification). Residual mantle modeled
1269 from primitive mantle McDonough and Sun (1995) and partition coefficients from Donnelly et al.
1270 (2004). Mantle depletion by melting is so efficient that the slab flux either strongly influences
1271 (MREE) or controls (LREE and more incompatible elements) the arc budgets of elements more
1272 incompatible than Ho. Only Ti and rare earth elements Ho to Lu remain mantle- controlled by
1273 mantle. See also Straub et al. (2014).

1274

1275 Figure 4: $^3\text{He}/^4\text{He}$ vs $\delta^{18}\text{O}$ of olivine phenocrysts in central MVB volcanic rocks. $\delta^{18}\text{O}$ recalculated
1276 to ratios in equilibrium melt [$\delta^{18}\text{O}_{\text{melt}} = \delta^{18}\text{O}_{\text{oliv}} + 0.088 * \text{SiO}_2 - 3.57$ after Bindeman (2008)]. $^3\text{He}/^4\text{He}$ of
1277 olivines are from Straub et al. (2011b). $^3\text{He}/^4\text{He}$ in MORB and continental crust from Farley et al.
1278 (1998) and O'Nions and Oxburgh (1988); $\delta^{18}\text{O}$ in mantle rocks from Bindeman (2008). Host
1279 magmas are basalts to andesites with up to 61 wt% SiO_2 .

1280

1281 Figure 5: $^{87}\text{Sr}/^{86}\text{Sr}$ vs $^{143}\text{Nd}/^{144}\text{Nd}$ of volcanic rocks and various crustal materials (Cenozoic
1282 MORB, trench sediment, continental basement). See Figure 1 for sample locations. Quaternary
1283 MORB is from the East Pacific Rise (PetDB, 2011). Large symbols denote volcanic rocks with
1284 olivines analyzed for $^3\text{He}/^4\text{He}$ and $\delta^{18}\text{O}$. Thick grey lines are simple mixing curves between AOC,
1285 mantle wedge (which have similar $^{87}\text{Sr}/^{86}\text{Sr}$ and Sr/Nd) and trench sediment (see text for
1286 discussion). The biotite gneiss of DSDP Site 489 is marked with a 'B'. Inset identifies the Old
1287 Texcal Flow and illustrates differences between calc-alkaline, high-La and Nb-rich magmas. For
1288 data sources see text.

1289

1290 Figure 6: **a.** $^{143}\text{Nd}/^{144}\text{Nd}$ vs. $^{176}\text{Hf}/^{177}\text{Hf}$, and **b.** $^{176}\text{Hf}/^{177}\text{Hf}$ vs. Nd/Hf of central MVB magmas and
1291 crustal materials (MORB, trench sediment, continental basement). See Figure 5 for symbols. Thick
1292 grey lines are simple mixing curves between AOC and trench sediment. Note that a mantle
1293 component would not affect the curvature of the mixing line, since mantle has similar $\text{Nd}/\text{Hf} \sim 4$
1294 (as well as Nd and Hf isotopic ratios) as the AOC. Mixing models must match arc data in both
1295 diagrams to be valid. The trench sediment fails as crust end member, while the
1296 offshore/Acapulco granodiorite lie in line with the AOC and compositions. Inset identifies the
1297 Old Texcal Flow and illustrates differences between calc-alkaline, high-La and Nb-rich magmas.
1298 For data sources see text.

1299

1300 Figure 7: **a.** $^{207}\text{Pb}/^{204}\text{Pb}$ vs. $^{206}\text{Pb}/^{204}\text{Pb}$, and **b.** $^{208}\text{Pb}/^{204}\text{Pb}$ vs. $^{206}\text{Pb}/^{204}\text{Pb}$ of central MVB magmas
1301 and crustal materials (MORB, trench sediment, continental basement). See Figure 5 for symbols.
1302 The thick grey line is a mixing curve (which are linear in Pb isotope space) through the central
1303 MVB magmas which are aligned with slab and mantle materials. The Cenozoic AOC (average
1304 ~ 18.2) fits much better as unradiogenic end member of the arc array than the more variable zero-
1305 age Quaternary MORB from the East Pacific Rise. Inset identifies the Old Texcal Flow and
1306 illustrates differences between calc-alkaline, high-La and Nb-rich magmas. For data sources see
1307 text.

1308

1309 Figure 8: Central MVB magmas: **a.** Bulk rock $^{143}\text{Nd}/^{144}\text{Nd}$ vs SiO_2 wt%. **b.** $^3\text{He}/^4\text{He}$ (olivine) vs
1310 SiO_2 wt% (bulk rock) with mixing curves from Straub et al. (2014). **c.** $\delta^{18}\text{O}$ (olivine) vs SiO_2 wt%
1311 (bulk rock), and **d.** $\delta^{18}\text{O}_{\text{melt}}$ [calculated from olivine after Bindeman (2008): $\delta^{18}\text{O}_{\text{melt}} = \delta^{18}\text{O}_{\text{oliv}} + 0.088$
1312 $* \text{SiO}_2$ (wt%) - 3.57] vs SiO_2 wt% (bulk rock). MORB field and fractional crystallization trajectory
1313 after Bindeman (2008). Mixing curves calculated with a crustal component $\text{SiO}_2 = 69$ wt% and
1314 $\delta^{18}\text{O} = 8-12$ ‰, and a mantle melt of $\text{SiO}_2 = 49$ wt% and $\delta^{18}\text{O} = 5.8$ ‰, respectively. See text for
1315 discussion.

1316

1317 Figure 9: $\delta^{18}\text{O}_{\text{melt}}$ vs. average fosterite of cores of olivine phenocrysts. Olivine concentrations are
1318 from Straub et al. (2011b; 2013a, this study; 2008). The $\delta^{18}\text{O}$ of continental crust is after Bindeman
1319 (2008).

1320

1321 Figure 10: Nd-Hf isotope and trace element mixing models. Valid models require mixing curves
1322 to pass through arc data in both the $^{143}\text{Nd}/^{143}\text{Nd}$ vs $^{176}\text{Hf}/^{177}\text{Hf}$ and Nd/Hf vs $^{176}\text{Hf}/^{177}\text{Hf}$ space. The
1323 models first calculate a 'bulk slab component' (AOC and bulk trench sediment, or AOC and
1324 granodiorite) shown as thick lines with 10% increments. The bulk slab component then mixes
1325 with the mantle wedge, shown as lines with only two tick marks (1% and 10%) for clarity (dashed
1326 - denotes curve for Nb-rich magmas). for . **a.-b.** Mixing between AOC and bulk trench sediment
1327 with preferential release of Hf from sediment by a factor of 7. **c.-d.** Mixing between AOC and
1328 bulk trench sediment with preferential release of Nd from AOC by a factor of 7. Either model
1329 produces misfits in the Nd/Hf vs $^{176}\text{Hf}/^{177}\text{Hf}$ space (except for the high-La basalts). **e.-f.** Mixing
1330 between AOC and granodiorite that have similar Nd/Hf ratios. Calc-alkaline and Nb-rich
1331 magmas require slightly different crustal and mantle end members in isotope space. Mixing
1332 model assumes primitive background mantle (Nd/Hf= 4.4) for Nb-rich magmas, and a residual
1333 mantle after by 5% melt extraction for calc-alkaline series (Nd/Hf=3.9). For details see text.

1334

1335 Figure 11: Idealized $^{87}\text{Sr}/^{86}\text{Sr}$ vs $^{143}\text{Nd}/^{144}\text{Nd}$ mixing model for calc-alkaline/high-La and Nb-rich
1336 magmas, respectively, with AOC, granodiorite and mantle wedge as end members. The models
1337 first calculate a 'bulk slab component'(AOC and bulk trench sediment, or AOC and granodiorite)
1338 which are shown as thick lines with 10% increments. The bulk slab component then mixes with
1339 the mantle wedge, shown as lines with only two tick marks (1% and 10%) for clarity (dashed -
1340 denotes curve for Nb-rich magmas). A successful model for the calc-alkaline series requires a
1341 component with increased $^{87}\text{Sr}/^{86}\text{Sr}$, depicted here to derive from subducted AOC.

1342

1343 Figure 12: Idealized $^{208}\text{Pb}/^{204}\text{Pb}$ vs. $^{206}\text{Pb}/^{204}\text{Pb}$ mixing model for a. calc-alkaline/high-La magmas,
1344 and b. Nb-rich magmas. The models first calculate a 'bulk slab component'(AOC and bulk trench
1345 sediment, or AOC and granodiorite) which are shown as thick lines with 10% increments (dashed
1346 - denotes curve for Nb-rich magmas in panel b). The bulk slab component then mixes with the
1347 mantle wedge, shown as lines with only two tick marks (1% and 10%) for clarity (dashed -
1348 denotes curve for Nb-rich magmas).

1349

1350 Figure 13: **a.** Percentage of slab-derived Pb in arc magmas vs. $^{206}\text{Pb}/^{208}\text{Pb}$. **b.** Percentage of slab-
1351 derived Sr in arc magmas vs. $^{87}\text{Sr}/^{86}\text{Sr}$. For calculation of slab-derived percentages see text. **c.**
1352 Percentage of slab-derived Nd in arc magmas vs. $^{143}\text{Nd}/^{143}\text{Nd}$. **d.** Percentage of slab-derived Hf in
1353 arc magmas vs. $^{176}\text{Hf}/^{177}\text{Hf}$.

1354

1355 Figure 14: Cartoon of central MVB subduction setting. Thermal structure model assumes mantle
1356 potential temperature of 1450°C and temperatures of ~700-800°C at about 110 km beneath the
1357 central MVB arc front, estimated from P-wave seismic tomography (Manea and Manea, 2011).

1358 Slab surface temperatures remains below sediment solidus ($\geq 1050^{\circ}\text{C}$, Behn et al., 2011)), but are
1359 conducive to the formation of thermochemical instabilities at the slab–mantle interface.

1360

1361 Figure 15: **a.-b.** Th/La *vs.* $^{143}\text{Nd}/^{144}\text{Nd}$, and **c.-d.** Nb/Ta *vs.* $^{143}\text{Nd}/^{144}\text{Nd}$ and mixing models for
1362 MVB magmas and their source components. Stippled lines outlines the range of the
1363 Acapulco/offshore granodiorites. The mixing models first calculate a 'bulk slab component' from
1364 AOC and eroded crust (thick lines with 10% increments). The bulk slab component then mixes
1365 with the mantle wedge, shown as lines with only two tick marks (1% and 10%) for clarity (dashed
1366 - denotes curve for Nb-rich magmas). Averages of major Earth reservoirs (right panels) are
1367 compiled from Plank (2004), McDonough and Sun (1995), Sun and McDonough (1989), Pfänder et
1368 al. (2007), and Muenker et al. (2003).

1369

1370 Figure 16: Nb (ppm) *vs.* Nb/Ta of central MVB arc volcanic rocks with range of MORB from Niu
1371 and Batiza (1997). Stippled lines mark average of Old Texcal Flow (proxy to subarc mantle wedge
1372 prior to subduction modification).

1373

1374

Table 1: Average percentages of slab contributions of Pb, Sr, Nd and Hf to calc-alkaline, high-La and Nb-rich magmas from trace element inversion.

	Sr	Pb	Nd	Hf
calc-alkaline magmas	87±4%	89±6%	74±8%	69±9%
<i>from mantle</i>	~13%	~11%	~26%	~31%
high-La series magmas	95±2%	96±2%	93±3%	73±7%
<i>from mantle</i>	~5%	~4%	~7%	~27%
Nb-rich magmas	49±10%	59±18%	47±16%	44±13%
<i>from mantle</i>	~51%	~41%	~53%	~56%

Table 2: Source components used for $^{143}\text{Nd}/^{143}\text{Nd}$ vs. $^{176}\text{Hf}/^{177}\text{Hf}$ isotope mixing models.

	$^{87}\text{Sr}/^{86}\text{Sr}$	$^{143}\text{Nd}/^{144}\text{Nd}$	$^{206}\text{Pb}/^{208}\text{Pb}$	$^{208}\text{Pb}/^{208}\text{Pb}$	$^{176}\text{Hf}/^{177}\text{Hf}$	Pb ppm	Sr ppm	Nd ppm	Hf ppm	Sr/Nd	Nd/Hf	Data Sources
Cenozoic MORB (AOC)	0.70350	0.51319	18.20	37.71	0.28321	0.62	123 ^a	10.28	2.57	11.9	4.00	this study
Bulk trench sediment	0.70825	0.51253	18.64	38.34	0.28290	38.9	208	28.5	2.48	7.3	11.5	(Cai et al., 2014; Plank, 2014)
Pelagic trench sediment	0.70837	0.51253	18.51	38.19	0.28294	66.2	284	51.2	2.51	5.6	20.4	(Cai et al., 2014; LaGatta, 2003; Verma, 1999b)
Terrigenous trench sediment	0.70858	0.51248	18.84	38.62	0.28278	20.9	179	19.8	2.43	9.1	8.15	(Cai et al., 2014; LaGatta, 2003; Verma, 1999b)
<i>calc-alkaline/high-La series</i>												
Background mantle wedge	0.70307	0.51300	18.71	38.41	0.28306	0.076	7.8	0.63	0.164	12.3	3.86	this study; residual of primitive mantle from McDonough and Sun (1995), after 3.5% melt extraction
Acapulco/offshore granodiorite	0.70460	0.51273	18.8	38.64	0.28291	13.6	294 ^b	32.8	5.70	9.0	5.75	this study.
<i>Nb-rich series</i>												
Background mantle wedge	0.70307	0.51300	18.71	38.41	0.28306	0.15	19.9	1.25	0.283	15.9	4.42	this study; primitive mantle from McDonough and Sun (1995)
intraplate seamount	0.70460 ^c	0.51273 ^c	18.8 ^c	38.64 ^c	0.2829 ^c	1.2	270	21.2	4.2	12.8	5.0	abundance data after Niu and Batiza (1997), Nb>10 ppm

a Model in Figure 14, uses increased Sr abundances, by factor of 3 for calc-alkaline series (Sr= 368 ppm; Sr/Nd=36), and by a factor of 2.5 for the NEAB (Sr= 306 ppm; Sr/Nd= 30).

b Model in Figure 14, uses increased Sr abundances, by factor of 4 (Sr= 1177 ppm; Sr/Nd=36)

c Isotope ratios estimated from trend of Nb-rich magmas in Sr-Nd-Pb-Hf isotope space

Table 3. Average percentages of Pb, Sr, Nd and Hf contributed from the mantle and the different slab reservoirs obtained from isotope modeling.

	Sr%	Pb%	Nd%	Hf%
Calc-alkaline/high-La series				
<i>mantle</i>	4	14	11	14
<i>AOC</i>	23	25	21	27
<i>Granodiorite</i>	73	61	68	59
Nb-rich magmas				
<i>mantle</i>	22	24	24	25
<i>AOC</i>	42	22	25	28
<i>Seamount</i>	37	54	51	46

Table 4: Source components used for Th/La vs. $^{143}\text{Nd}/^{144}\text{Nd}$ and Nb/Ta vs. $^{143}\text{Nd}/^{144}\text{Nd}$ mixing models.

	$^{143}\text{Nd}/^{144}\text{Nd}$	Th ppm	La ppm	Nb ppm	Ta ppm	Th/La	Nb/Ta	Data Sources
Cenozoic MORB (AOC)	0.51319	0.33	4.9	4.55	0.285	0.07	15.6	this study
Bulk trench sediment	0.51253	6.00	36.3	8.65	0.557	0.17	15.5	(Cai et al., 2014; Plank, 2014)
Pelagic trench sediment	0.51253	5.51	56.4	8.09	0.44	0.08	18.2	(Cai et al., 2014; LaGatta, 2003; Verma, 1999b)
Terrigenous trench sediment	0.51248	7.50	20.4	11.04	0.84	0.32	13.2	(Cai et al., 2014; LaGatta, 2003; Verma, 1999b)
Acapulco/offshore granodiorite	0.51270-0.51276	1.1-13.6	15.1-37.1	15.7-30.9	1.36-1.58	0.07-0.37	11.5-19.6	this study.
<i>calk-alkaline/high-La series</i>								
Background mantle wedge	0.51300	0.0011	0.105	0.02	0.0012	0.01	16.22	this study; residual of primitive mantle from McDonough and Sun (1995), after 3.5% melt extraction
<i>Nb-rich magmas</i>								
Background mantle wedge	0.51300	0.0795	0.648	0.6	0.037	0.12	16.22	this study; primitive mantle from McDonough and Sun (1995)

Figure

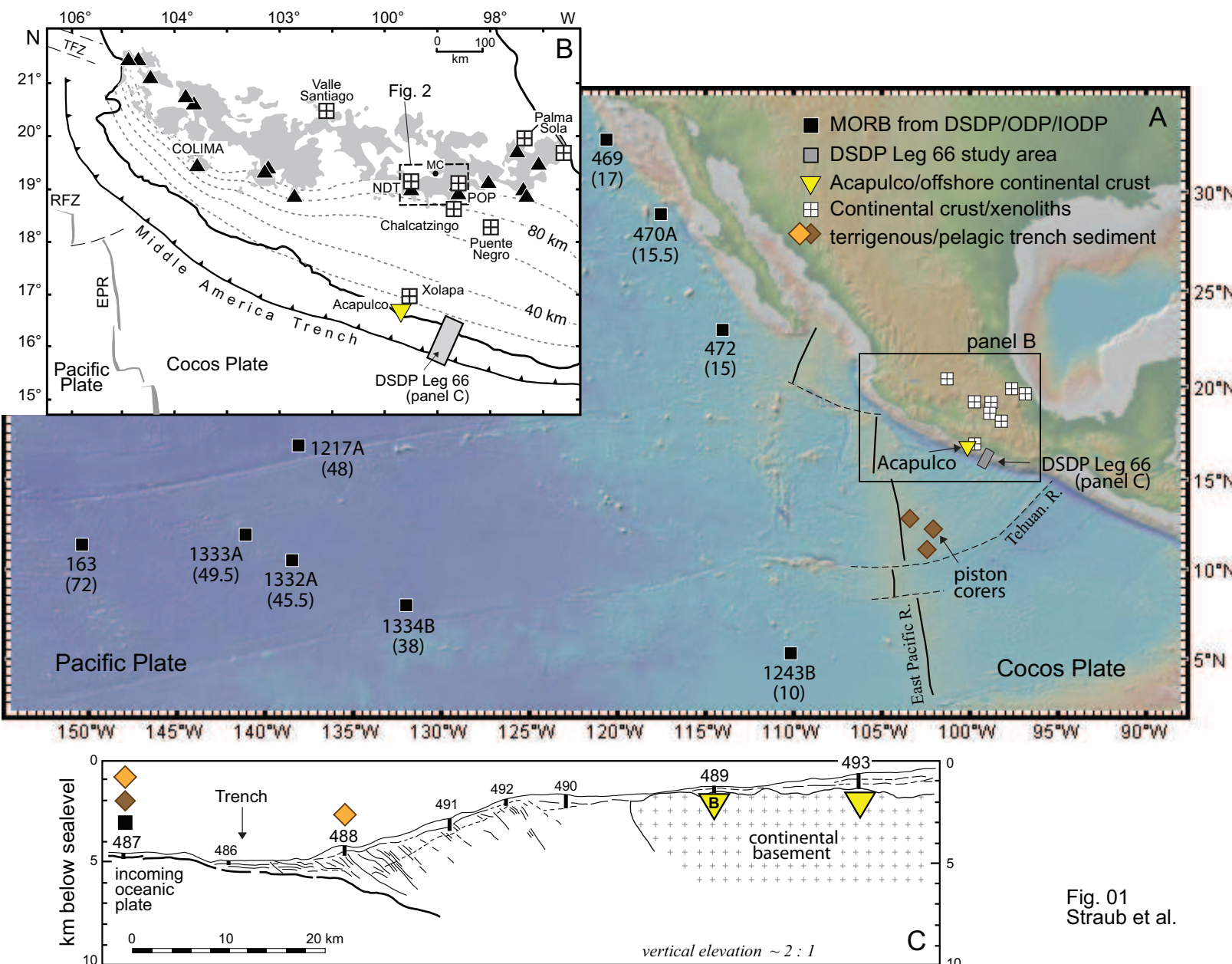


Fig. 01
Straub et al.

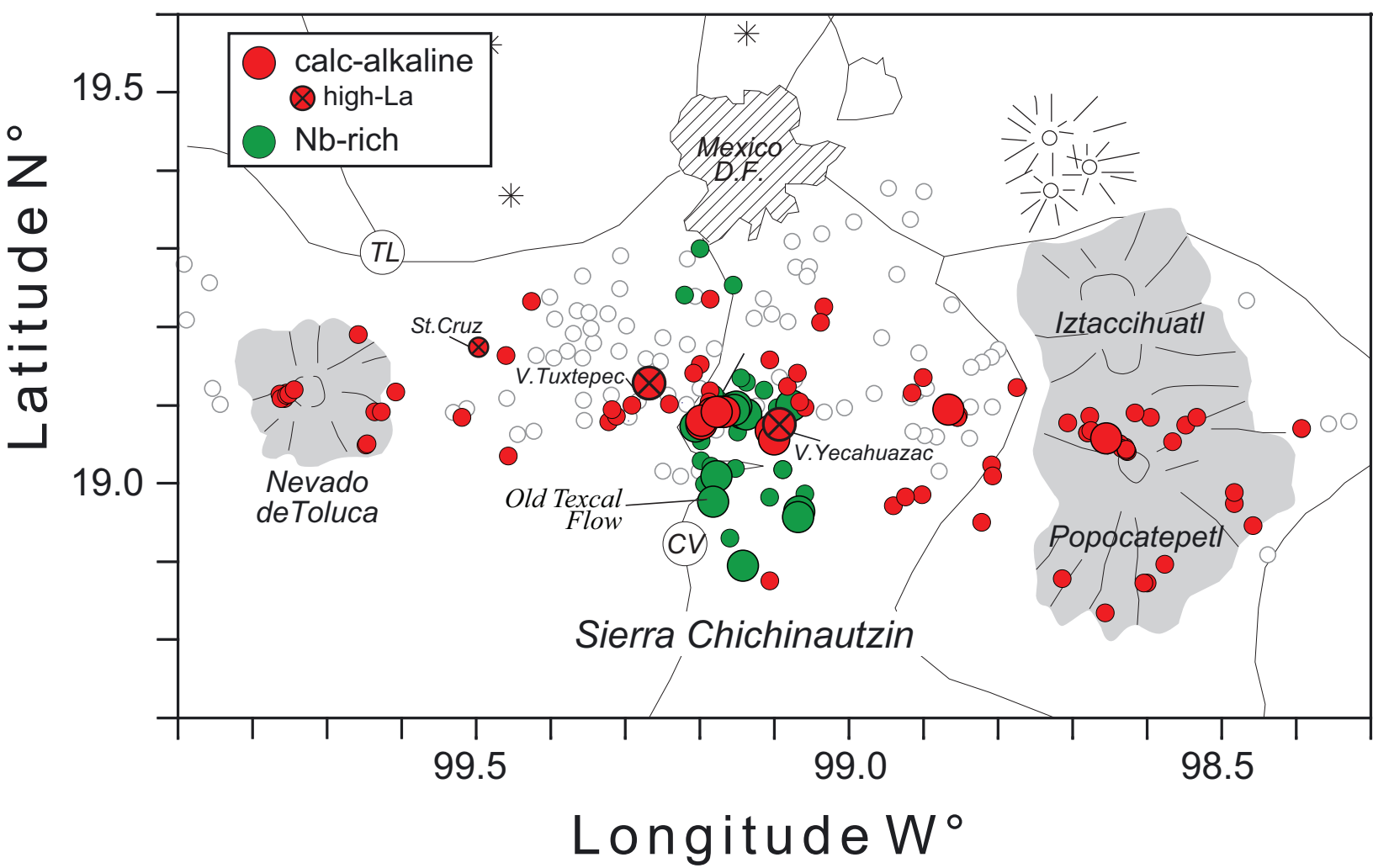


Fig. 02
Straub et al.

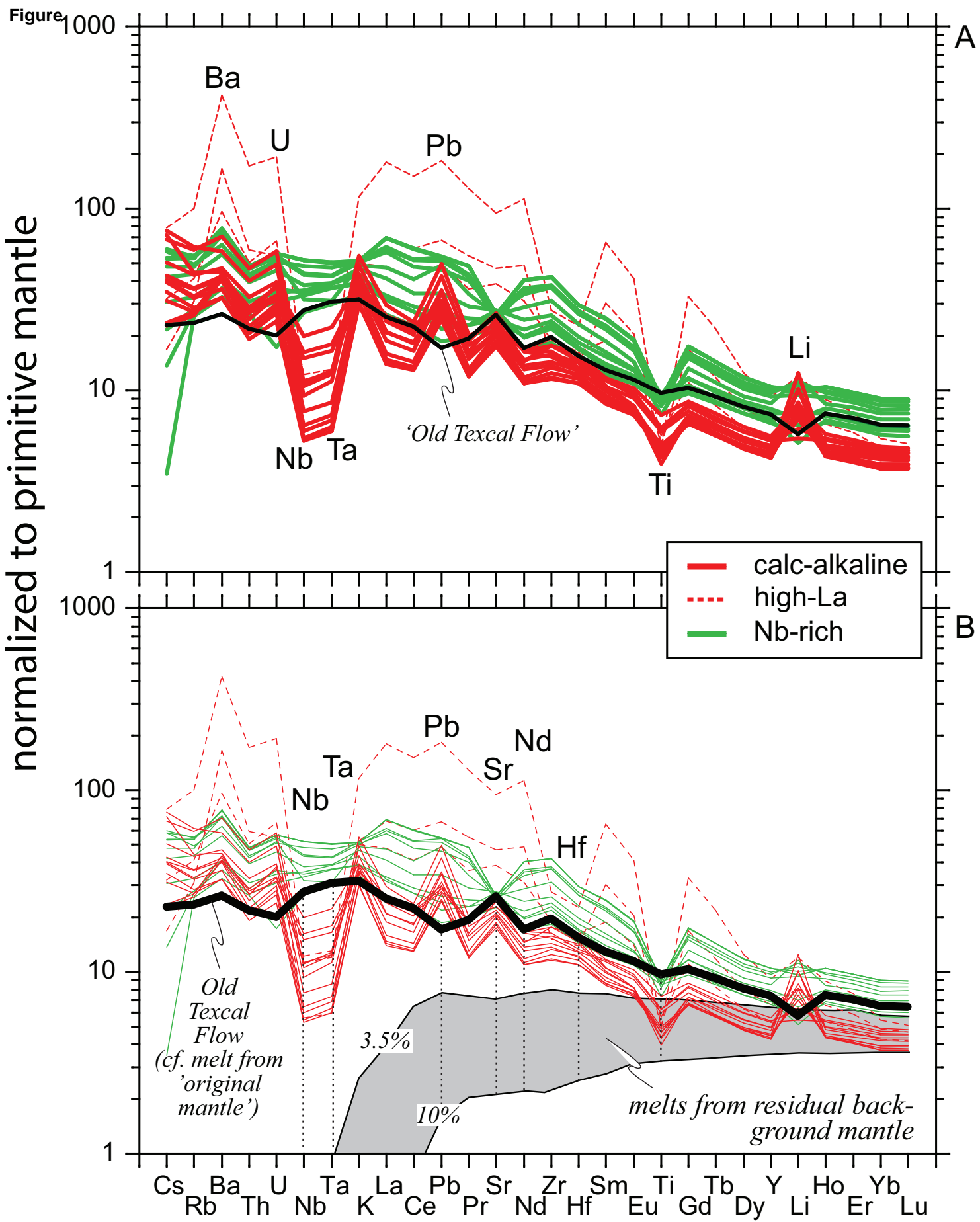


Fig. 03
Straub et al.

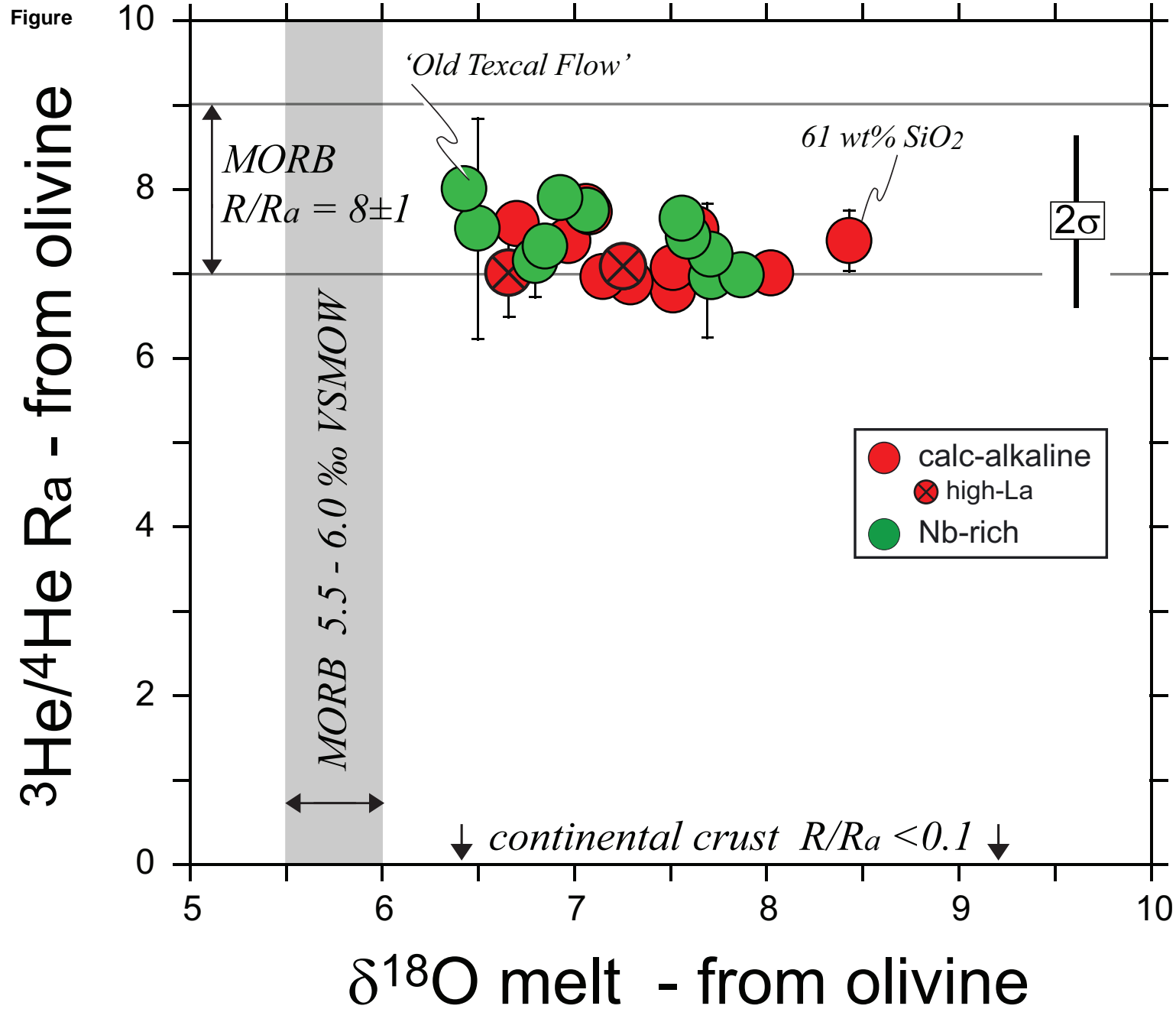


Fig. 04
Straub et al.

Figure

- calc-alkaline
- ⊗ high-La
- Nb-rich
- ◆ terrigenous
- ◆ pelagic
- Cenozoic AOC
- ⊕ continental basement
- ▼ Acapulco/offshore granodiorite/b. gneiss

$^{143}\text{Nd}/^{144}\text{Nd}$

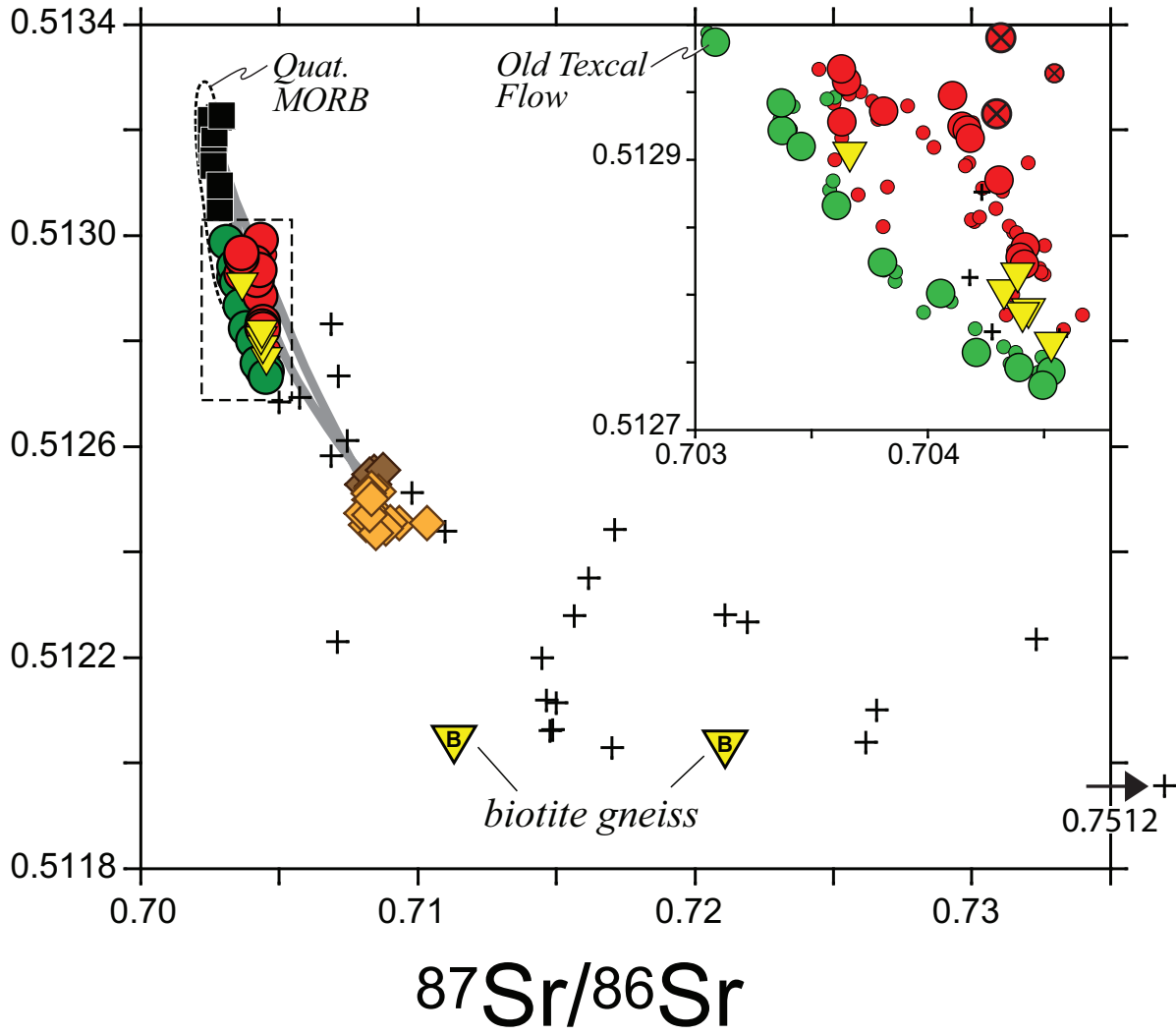
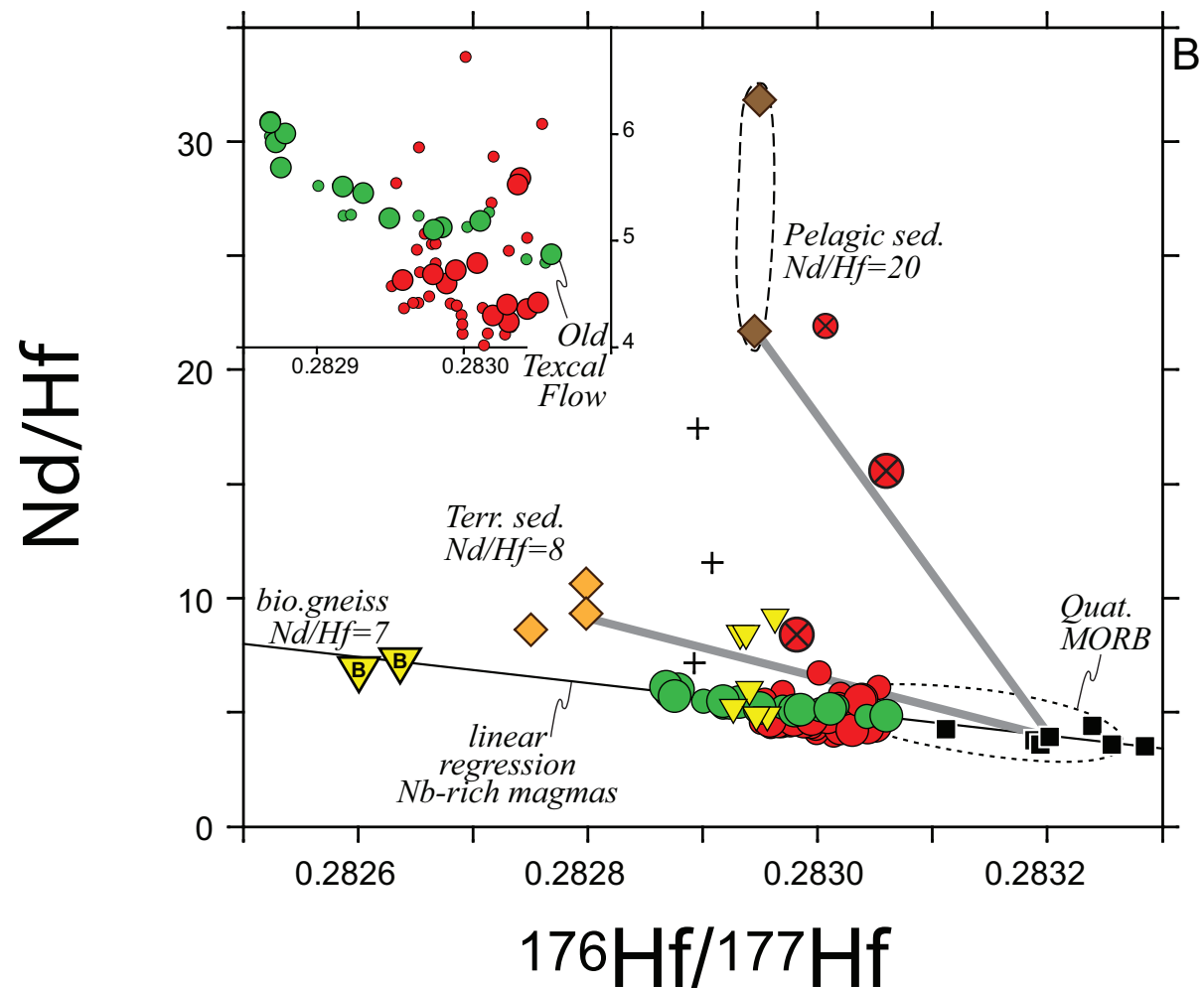
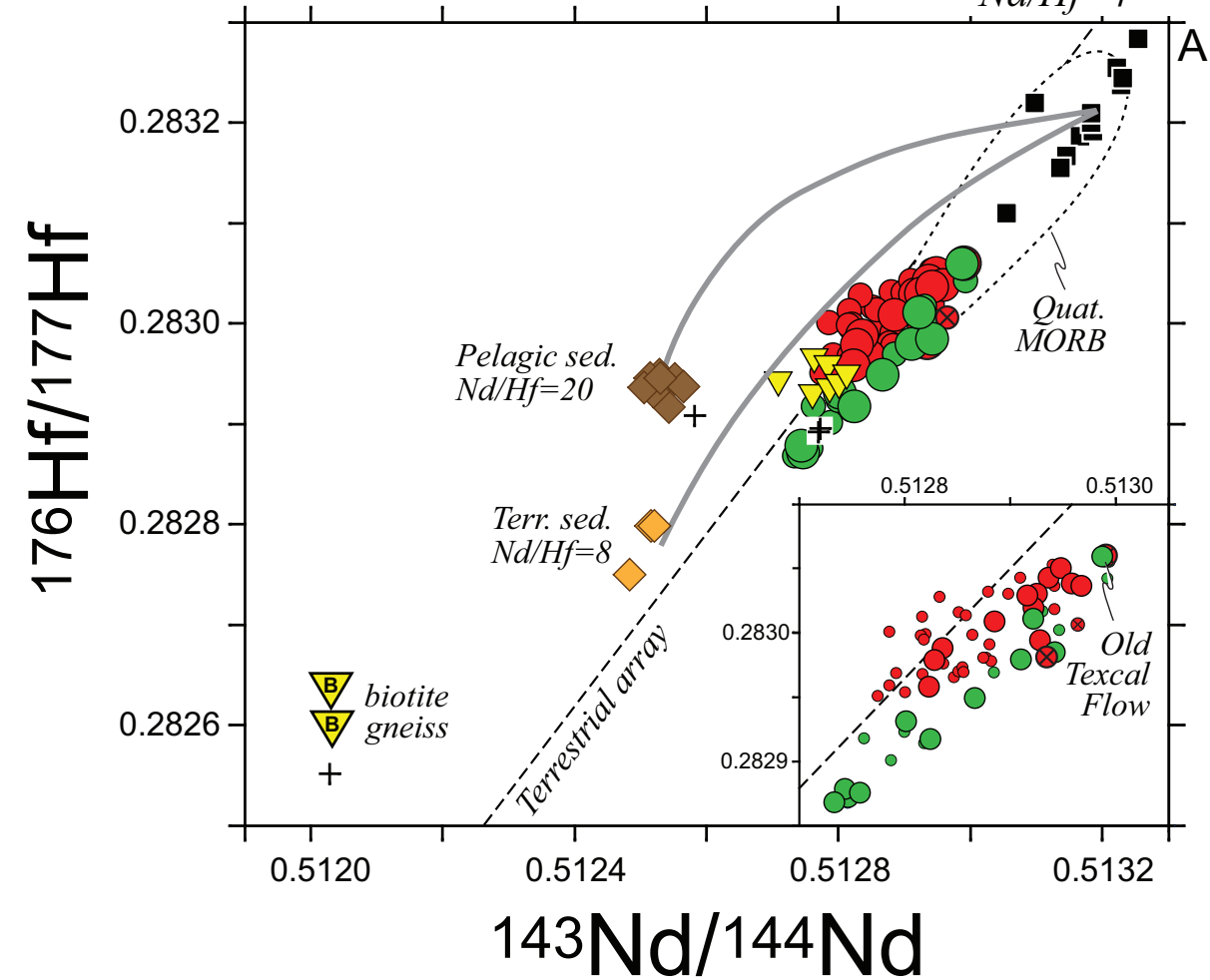
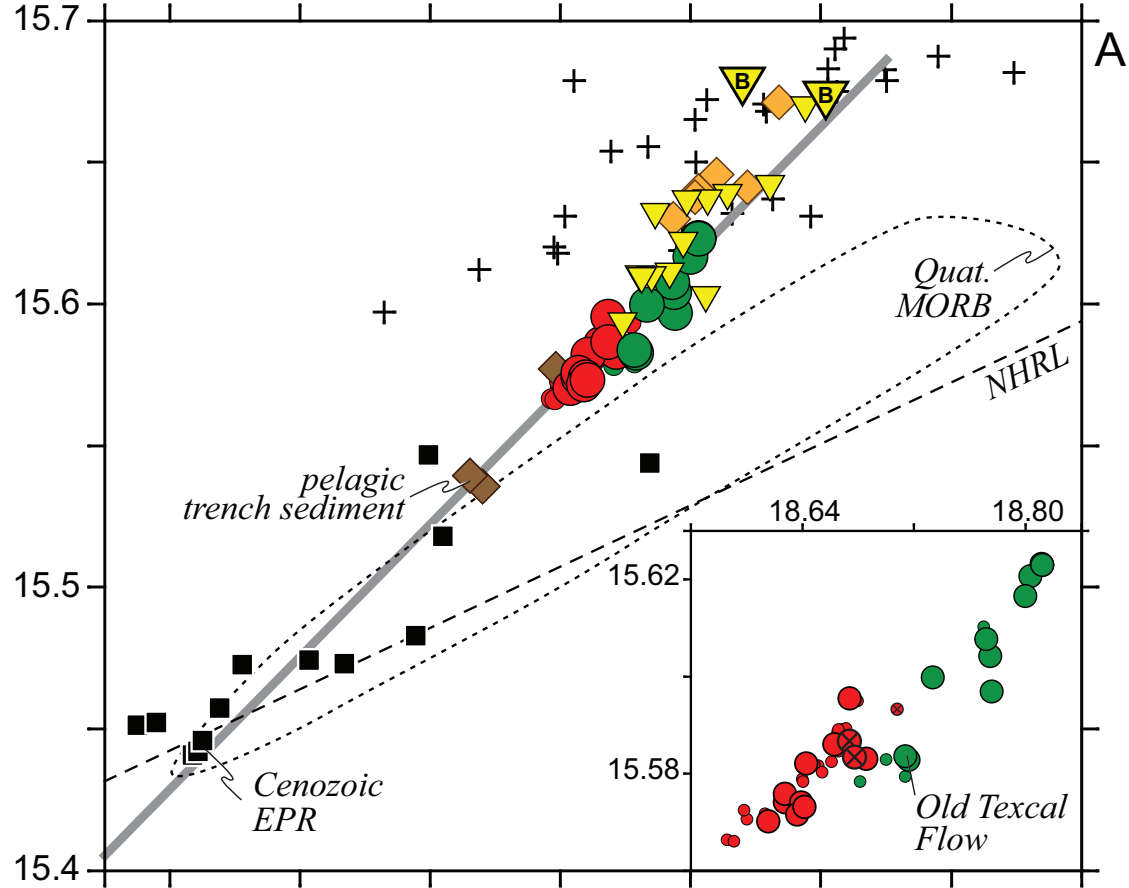
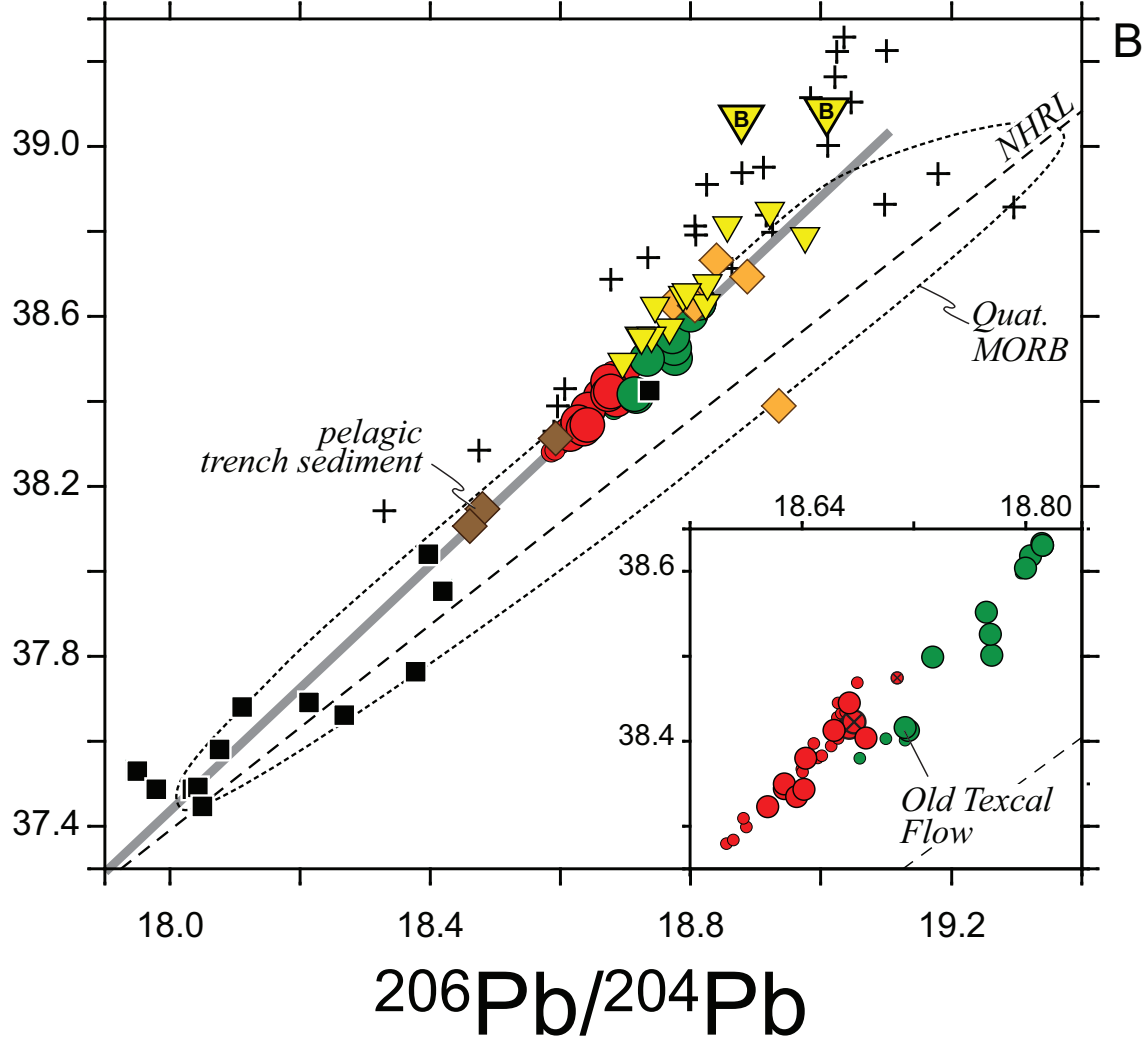
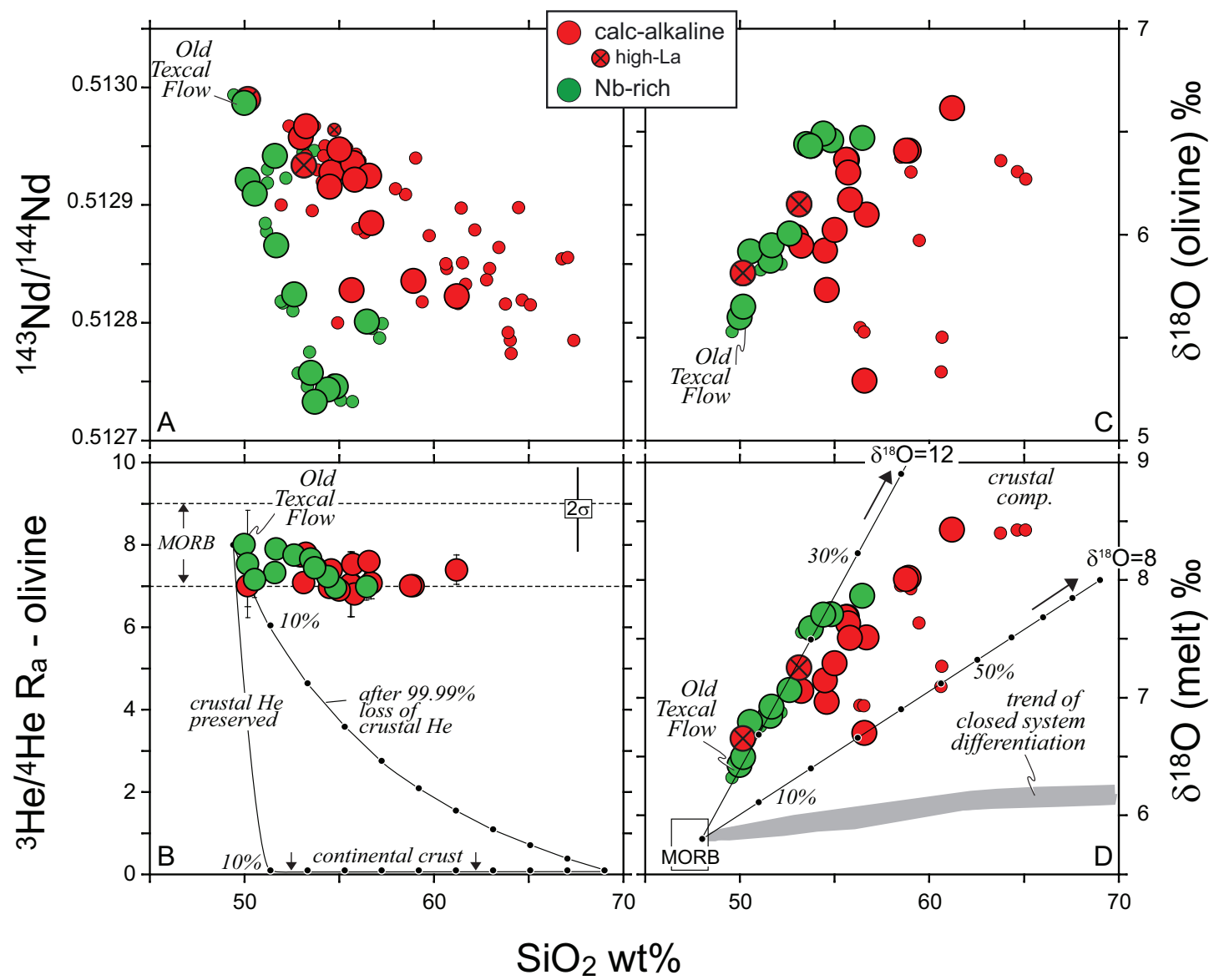


Fig. 05
Straub et al.



Figure

 $^{207}\text{Pb}/^{204}\text{Pb}$  $^{208}\text{Pb}/^{204}\text{Pb}$  $^{206}\text{Pb}/^{204}\text{Pb}$ Fig. 07
Straub et al.



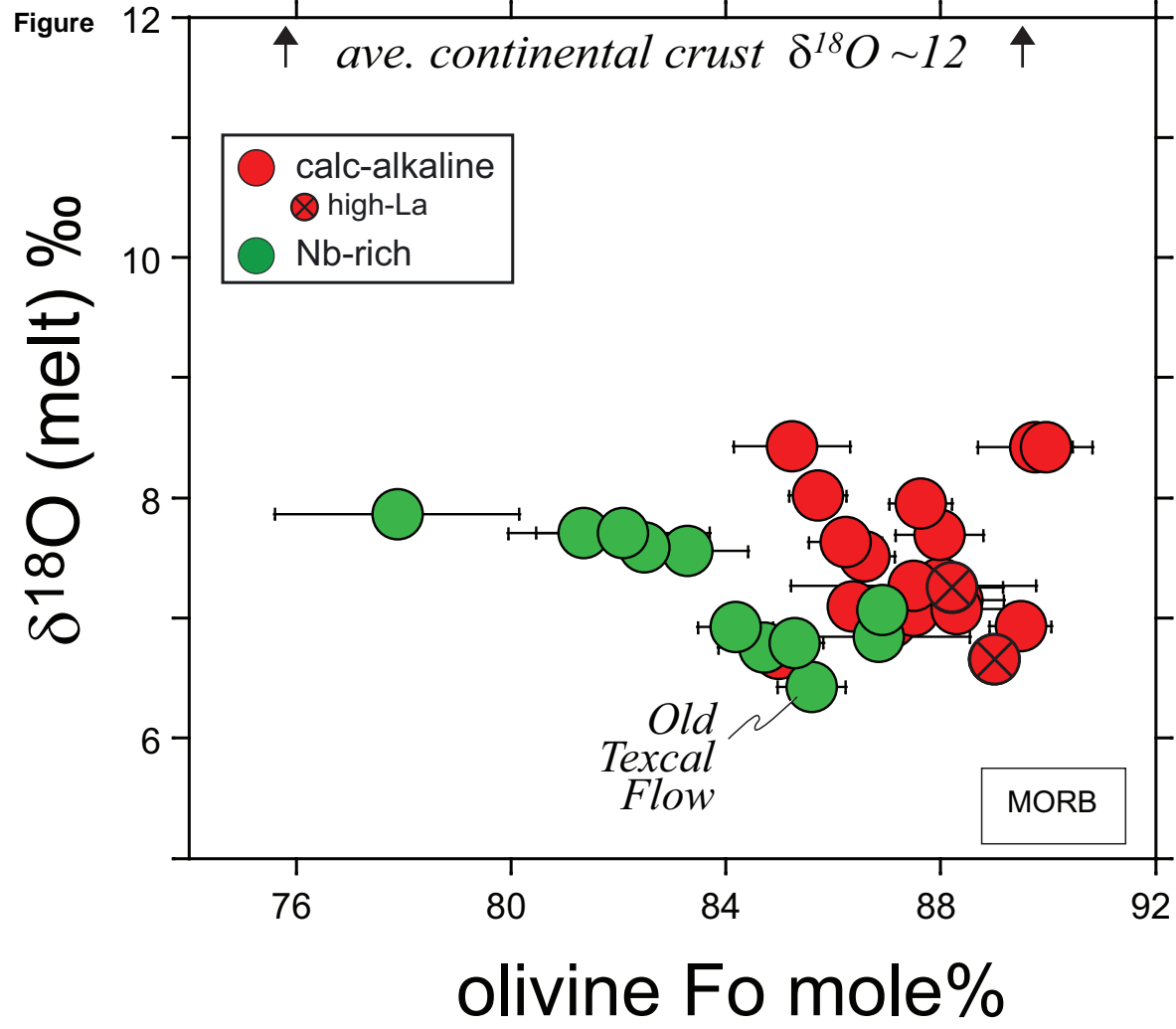
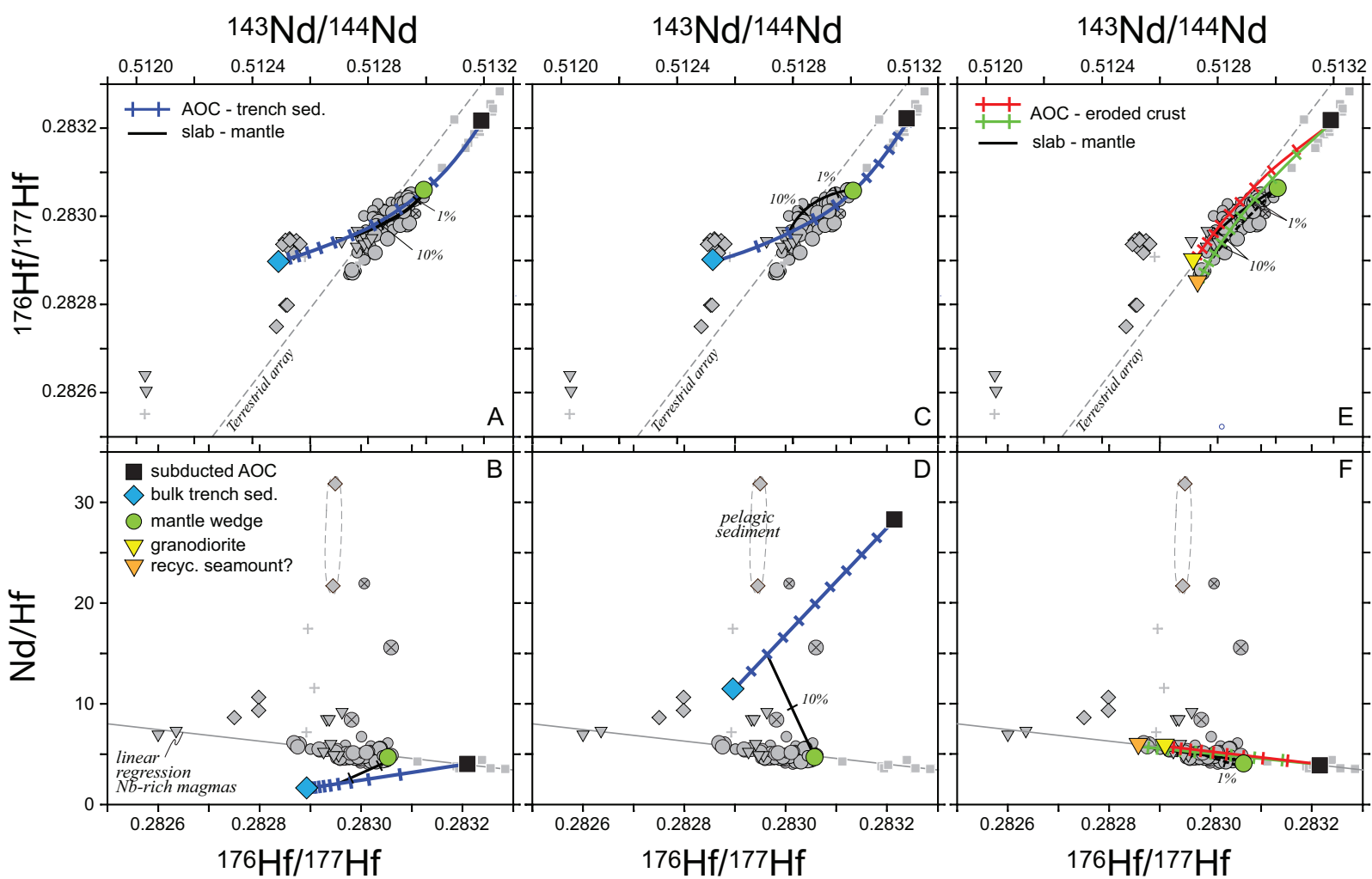


Fig. 09
Straub et al.



Figure

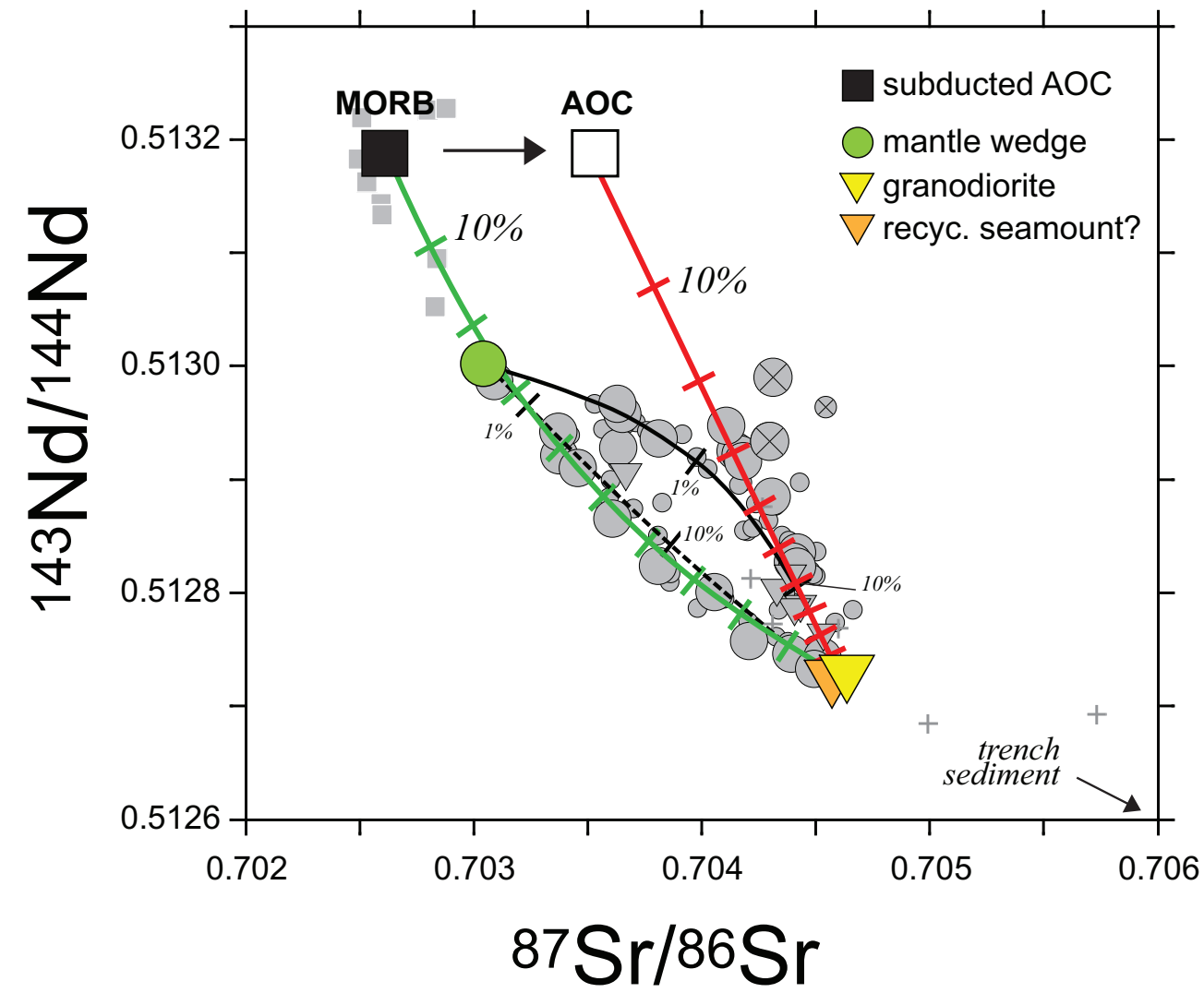


Fig. 11
Straub et al.

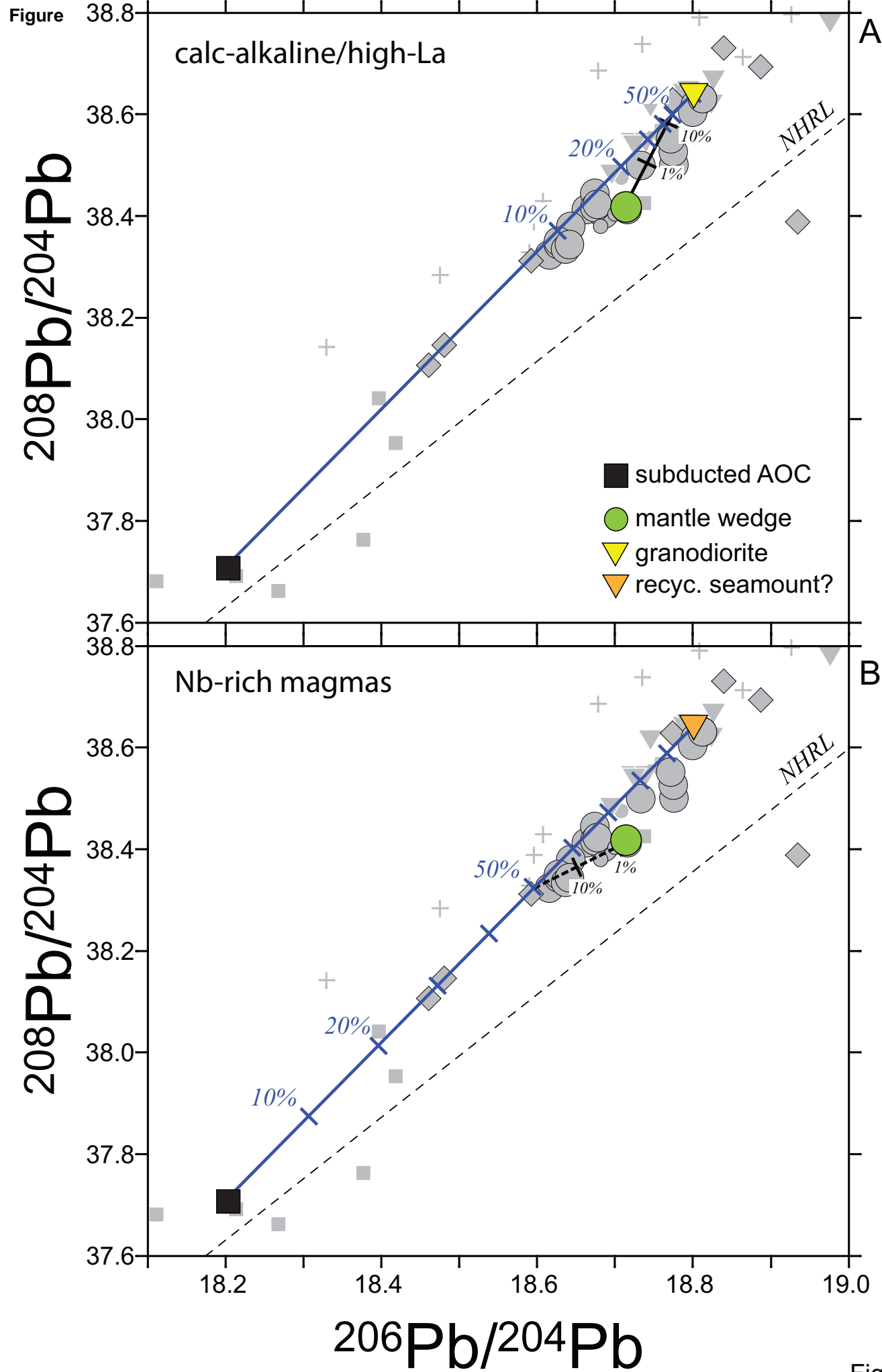


Fig. 12
Straub et al.

Figure

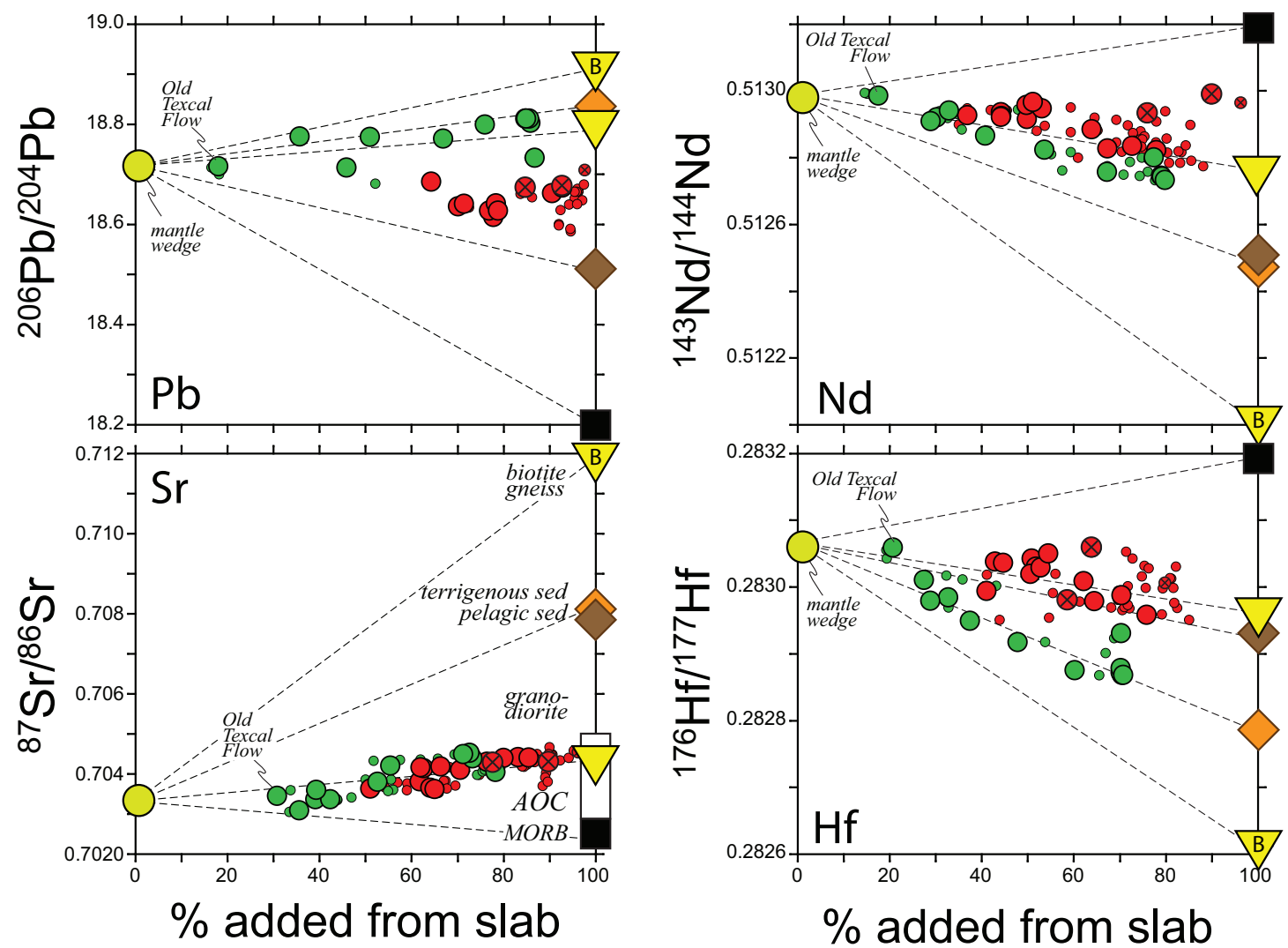


Fig. 13
Straub et al.

Figure

Depth (km below seafloor)

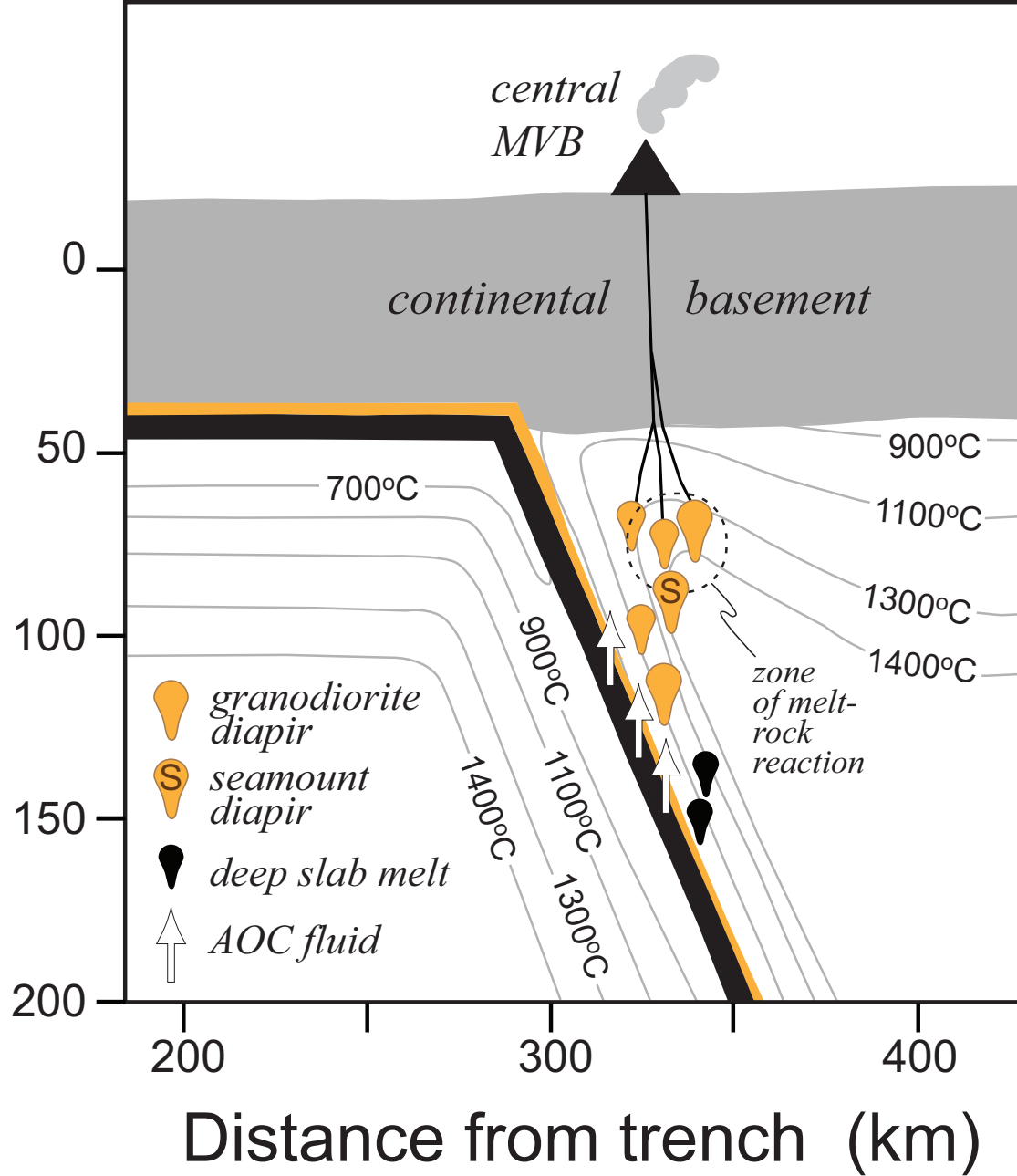
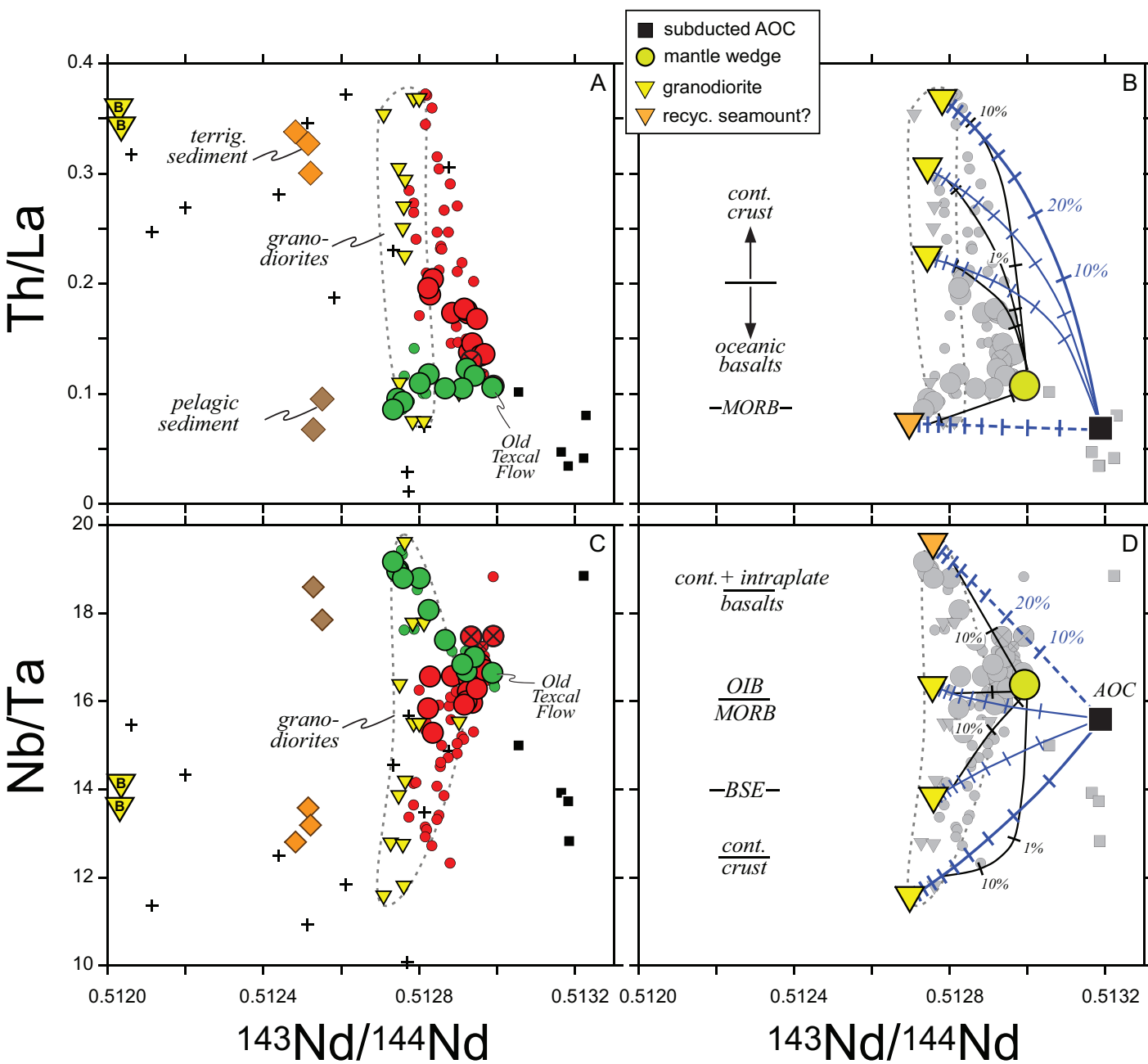


Fig. 14
Straub et al.



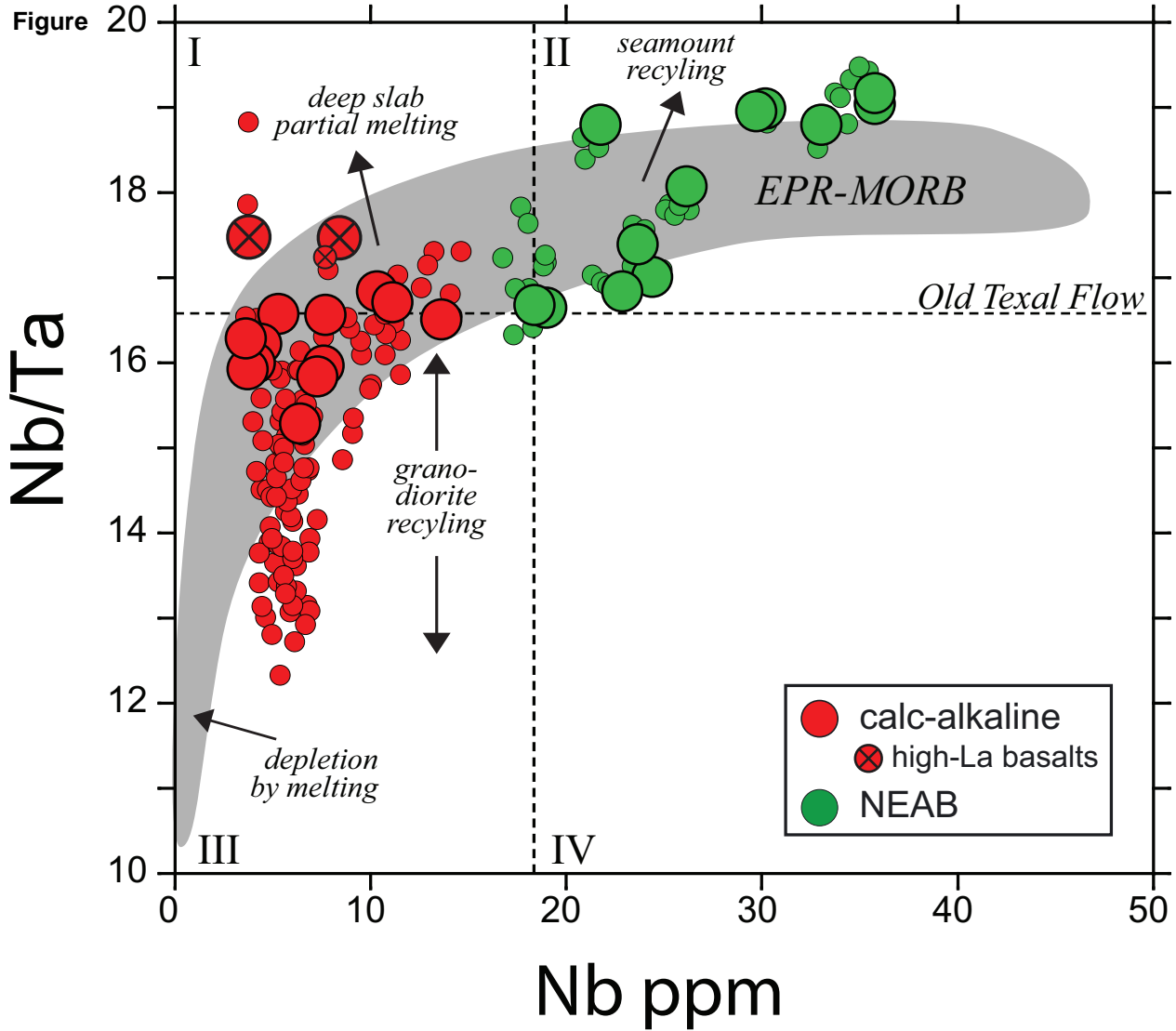


Fig. 16
Straub et al.

Electronic Annex

[Click here to download Electronic Annex: Appendix_A_B_rev2.pdf](#)

Electronic Annex

[Click here to download Electronic Annex: Appendix Table 1.xls](#)

Electronic Annex

[Click here to download Electronic Annex: Appendix Table 2.xls](#)

Electronic Annex

[Click here to download Electronic Annex: Appendix Table 3.xls](#)

Electronic Annex

[Click here to download Electronic Annex: Appendix Table 4.xls](#)

Electronic Annex

[Click here to download Electronic Annex: Appendix Table 5.xls](#)

Electronic Annex

[Click here to download Electronic Annex: Appendix Table 6.xls](#)

Electronic Annex

[Click here to download Electronic Annex: Appendix Table 7.xls](#)

Electronic Annex

[Click here to download Electronic Annex: Appendix Table 8.xls](#)

Electronic Annex

[Click here to download Electronic Annex: Appendix Table 9.xls](#)

Electronic Annex

[Click here to download Electronic Annex: Appendix_Table 10.xls](#)